Chapter 1
Deformation and Fracture of Perfect Crystals

Perfect crystals constitute an idealization of real single crystals that always contain some crystal defects. This holds even for almost perfect single crystals, so-called whiskers, where the presence of an equilibrium concentration of vacancies is inevitable. On the other hand, the mechanical behaviour of perfect crystals can be very successfully simulated and predicted by theoretical *ab initio* approaches based on electronic structure calculations. Because many of the crystallographic, elastic, electric, magnetic and thermodynamic characteristics of crystals do not depend on crystal defects, the *ab initio* results can still be experimentally verified. The practical importance of such studies lies in several general aspects.

First, knowledge of the behaviour of perfect crystals clearly identifies the role of crystal structure and chemical composition. This enables us to separate the role of defects due to the difference in the mechanical behaviour of perfect and real crystals. Second, the ideal (theoretical) strength of perfect crystals of a particular chemical composition represents an upper bound of the strength of solids. Consequently, engineers can see the gap remaining between the strength of contemporary high-strength materials and that of the theoretical limit. Third, the models of processes of dislocation creation near stress concentrators such as cracks in perfect crystals provide us with lower bounds of macroscopic characteristics used in fracture mechanics. Thus, the *ab initio* results yield both upper and lower benchmarks defining physically possible ranges of mechanical characteristics of engineering materials. Fourth, the characteristics of ideal crystals can be utilized in multiscale models of deformation and fracture processes of engineering materials. Finally, these results can be used as fitting data for the construction of sophisticated semi-empirical interatomic potentials that are utilized for prediction of the behaviour of extended defects in real crystals and polycrystals.

All of the above-mentioned aspects are demonstrated in the three sections of this chapter devoted to the mechanical behaviour of perfect crystals. In the first section, the application of *ab initio* methods to calculations of elastic stress-strain response and, particularly, to the determination of ideal

strength under various loading conditions is demonstrated. One should note that these concepts are, in fact, two scale models based on both electronic and atomic structures. Section 1.2 deals with another important problem concerning the physics of brittle/ductile behaviour of perfect crystals. The models are three-scale approaches dealing with electronic, atomic and crystallographic structures of crystals. The third section illustrates the modelling of nanoindentation tests with regard to the physical interpretation of pop-ins observed at the end of the elastic part in the force-indentation depth diagram. These multiscale models couple electronic, atomic, crystallographic and continuum approaches to provide a unique tool for experimental measurements of the ideal shear strength.

1.1 Ideal Strength of Solids

The strength of any solid has an upper limit called the ideal (theoretical) strength (IS). This value corresponds to the failure of an infinite perfect single crystal loaded in a defined mode. The strength of engineering materials is usually controlled by nucleation and propagation of dislocations and/or microcracks. If such defects were not present, the material would only fail when the IS is reached. Until recently loads of this magnitude were only approached in studies of the mechanical behaviour of whiskers of very pure metals and semiconductors [1,13,14]. Starting from the beginning of the last century, there has been a more or less continuous effort expended in order to obtain theoretical and experimental data concerning IS of various solids. The IS values set an upper limit to the envelope of attainable stresses and its knowledge enables us to assess the gap remaining to upper strength values of advanced engineering materials in each period of time. However, this is not the only reason for IS investigation. From the theoretical point of view, the IS plays a decisive role in the fundamental theory of fracture. For example, the stress necessary for nucleation of a dislocation loop can be identified with the shear IS value. This has been proved most eloquently by nanoindentation experiments (see e.g., [15–18]) which suggest that the onset of yielding at the nanoscale is controlled by a homogeneous nucleation of dislocations in a small, dislocation free, volume under the nanoindenter, where the stresses approach the shear IS. Similarly, the local stress needed for unstable propagation of a cleavage crack should overcome the value of the tensile IS [19–22]. The ratio of shear and tensile IS expresses a tendency of the crystal matrix to become brittle or ductile [23–25] (see Section 1.2). The values of IS may also be used in the construction or checking of semi-empirical interatomic potentials. From the practical point of view, the shear IS appears to control both the onset of fracture and the dislocation nucleation in defect-free thin films and, in particular, in nano-structured materials that are currently being developed. Perfect single crystal wires (whiskers) are used as reinforcements in advanced

composite materials and large metallic and ceramic single crystals start to be important in special engineering components, e.g., in turbine blades [26].

Section 1.1.1 provides a picture of the historical development including remarks on sophisticated calculation methods. The principles of *ab initio* methods and stability procedures, utilized in recent computations, are presented in Section 1.1.2. Some results of *ab initio* calculations of IS under simple loading modes reported in our works are outlined in Section 1.1.3. Section 1.1.4 is dedicated to IS of crystals under multiaxial loading. An analysis of mechanical properties of ideal nanocomposites is outlined in Section 1.1.5. A brief discussion concerning the influence of lattice defects and temperature on the crystal strength is presented in the last subsection.

Section 1.1 is complemented by two appendices focused on *ab initio* methods and mixed-mode criteria of crack stability.

1.1.1 From Classics to Recent Concepts

For every particular loading, the stress state is characterized by six stress tensor components and, consequently, an infinite number of ideal strengths exists for a given crystal. For practical reasons, therefore, the IS was usually evaluated only for several special cases of loading, each defined by a single value of the stress tensor component, specifically, for the uniaxial tensions and compressions along various crystallographic directions, the isotropic (hydrostatic) tension and compression and for the pure shear in certain planes and directions. The respective IS values denoted here as $\sigma_{iut}, \sigma_{iuc}, \sigma_{iht}, \sigma_{ihc}$ and τ_{is} cover, to a reasonable degree, the most important cases occurring in the engineering practice.

1.1.1.1 Classical Theories

Historically the first calculations of τ_{is} were performed in 1926 by Frenkel [27]. The model of an ideal crystal subjected to block-like shear is, along with the related behaviour of the shear stress τ under applied shear deformation, expressed by the plane shift s in Figure 1.1. The values of ideal shear strength for the block-like model will be denoted $\tau_{is,b}$. The $\tau(s)$ dependence was assumed to be of a sinusoidal shape.

According to specification of variables in Figure 1.1, the stress behaviour could be described by the relation

$$\tau = \tau_{max} \sin \frac{2\pi}{a} s.$$

For a small shift ($\sin \frac{2\pi}{a} s \approx \frac{2\pi}{a} s$), the shear modulus should be $G = \mathrm{d}\tau/\mathrm{d}\xi$, where $\xi = s/b$. Since $\tau_{is,b} = \tau_{max}$ this leads to

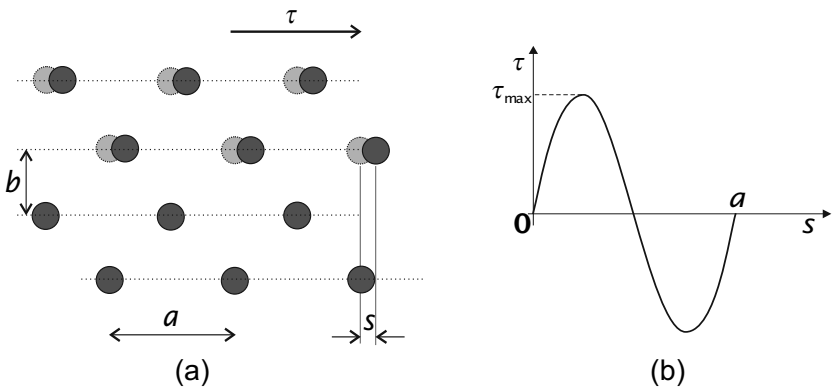

Figure 1.1 (a) Model of a block-like shear deformation (*dark spheres* represent atomic positions within the upper block, that is, as a whole, shifted by s towards the lower block along the shear plane, *light spheres* show their original positions), and (b) shear stress τ as a function of the shift s of two adjacent planes

$$\tau_{is,b} = \frac{Ga}{2\pi b}. \tag{1.1}$$

Equation 1.1 gave values $\tau_{is,b} \approx \frac{1}{9}G$ for the $\{111\}\langle 11\bar{2}\rangle$ shear of face centred cubic (fcc) metals, and $\tau_{is,b} \approx \frac{1}{5}G$ for $\{110\}\langle 1\bar{1}1\rangle$ shear of bcc metals as well as for the $\{111\}\langle 1\bar{1}0\rangle$ shear of fcc metals. Because the yield stress of real crystals was found to be about three orders lower, the only plausible explanation of this discrepancy was the presence of line defects (dislocations). Thus, the Frenkel's result created a milestone for a development of the dislocation theory.

First attempts to compute the ideal strength in uniaxial tension σ_{iut} were performed by Polanyi [28] and Orowan [29]. They were based on an assumption of tearing fracture of a stretched crystal along a crystallographic plane. Forces between two adjacent atomic planes of a perfect solid vary with the interplanar distance as in Figure 1.2. This dependence was approximated by a sinusoidal function

$$\sigma = \sigma_{\max} \sin \pi \frac{x - a_0}{d}$$

and the expected deviation from this trend for high strain values was neglected. The function was parametrized according to the following assumptions: 1) the work of deformation per unit area corresponds to energy 2γ of the two new surfaces

$$\int_{a_0}^{a_0+d} \sigma \mathrm{d}x = 2\gamma;$$

and 2) in the vicinity of the equilibrium state ($x = a_0$), the stress is proportional to Young's modulus and the relation $E = \dfrac{\mathrm{d}\sigma}{\mathrm{d}\varepsilon}$ must be valid for the strain $\varepsilon = \dfrac{x - a_0}{d}$. Then, the maximum value of the tensile stress can be simply evaluated as

$$\sigma_{iut} = \sqrt{\frac{E\gamma}{a_0}}. \tag{1.2}$$

The corresponding ideal tensile (tear) strengths of metals are mostly very high (several tens of GPa).

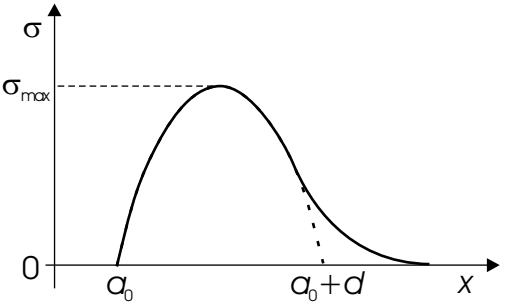

Figure 1.2 Stress as a function of the distance between atomic planes

Mackenzie presented in 1949 a more extended study of the shear IS based on a variation of potential energy U per unit area of a shear plane with the plane shift s [30]. The shear stress can be calculated from the energy U as

$$\tau = \frac{\mathrm{d}U}{\mathrm{d}s}. \tag{1.3}$$

From this point of view, the Frenkel's approach described above refers only to the first two terms in the Fourier series for $U(s)$. Therefore, Mackenzie took further terms into consideration. This theory gave a very low value $\tau_{is,b} \approx \frac{1}{30}G$ for $\{111\}\langle 11\bar{2}\rangle$ shear in fcc lattice [30]. As found by Šandera and Pokluda [31], however, some assumptions used in that theory were not physically legitimate. Indeed, more recent calculations [31, 32] based on more sophisticated atomistic approaches confirmed a much better validity of Frenkel's estimation.

Further IS calculations were performed by means of so-called empirical interatomic potentials [33]. Most of them used an analogy to Equation 1.3. The potential energy U was calculated as a sum of pair-potentials of various kinds such as the Morse potential, the Lennard–Jones potential, etc. (e.g., [23, 24,34–36]). As an example, some results of calculations of σ_{iht} are introduced in Section 1.1.3.

1.1.1.2 *Ab initio* Methods

Nowadays, so-called *ab initio* (or first principle) approaches enable us to compute the crystal energy in a very accurate manner. This particularly holds for single crystals of pure elements or compounds, crystals with periodical arrangements of atoms of various kinds and also for local crystal defects. These methods utilize the density functional theory [37, 38] in which the problem of many interacting electrons is transformed into a study of single electron motion in an effective potential. A brief description of principles of such methods is presented in Appendix A.

Most probably, the first *ab initio* calculation of the uniaxial IS σ_{iut} was that of Esposito *et al.* [39] for the copper crystal. However, these authors did not perform relaxations of atomic positions inside the loaded crystal in directions perpendicular to the loading axis (Poisson's type of expansion or contraction). Probably the first *ab initio* simulation of a tensile test that included the relaxation in perpendicular directions to the loading axis was performed by Price *et al.* [40] for TiC along the [001] axis. Later, σ_{iut} was calculated for [001] and [111] loading axes for a variety of cubic crystals by Šob *et al.* [41–43]. Kitagawa and Ogata [44,45] studied the tensile IS of Al and AlN but also did not include the Poisson's contraction. Further calculations of σ_{iut}, performed for α-SiC, diamond, Si, Ge, Mo, Nb and Si_3N_4, have already taken that effect into account by allowing a transversal relaxation of atoms [46–51].

The values $\tau_{is,b}$ of the shear IS were first calculated by Paxton *et al.* [32] for V, Cr, Nb, Mo, W, Al, Cu and Ir. The values τ_{is}^{*} calculated according to the model of a uniform shear (see Figure 1.3) were later reported by Moriarty *et al.* [52,53] for Mo and Ta. These calculations did not include any relaxations. Recently, the relaxed values of τ_{is} were calculated for many crystals such as TiC, TiN, HfC, Mo, Nb, Si, Al, Cu and W by groups of Morris *et al.*, Kitamura *et al.* and Pokluda *et al.* [54–58]. In these models, the interplanar distance was relaxed towards the minimum energy during deformation. More advanced models also enabled relaxations of the arrangement of atomic positions within the planes [48, 59] – see also Sections 1.1.2 and 1.1.3.

Since 1997, *ab initio* calculations of σ_{iht} have been performed by Pokluda *et al.* [60–62] and other authors (e.g., [63]). Since spherical symmetry was maintained during deformation, the relaxation procedures were not necessarily applied in these models.

In the majority of older studies on IS, the deformation process was assumed to proceed in a stable manner until the applied stress reached its maximum value. This means that the crystal failed in the same mode in which it was originally deformed from the very beginning. However, this assumption was disputed in many works [64–66]. Under both tensile and compressive loadings, the shear stresses in some slip systems can exceed their critical values (corresponding to the related τ_{is}) well before the stress reaches its maximum. This was also observed in tensile tests on whiskers [30, 33]. Indeed, some of the whiskers evidently failed by shear across some favourable crystallographic

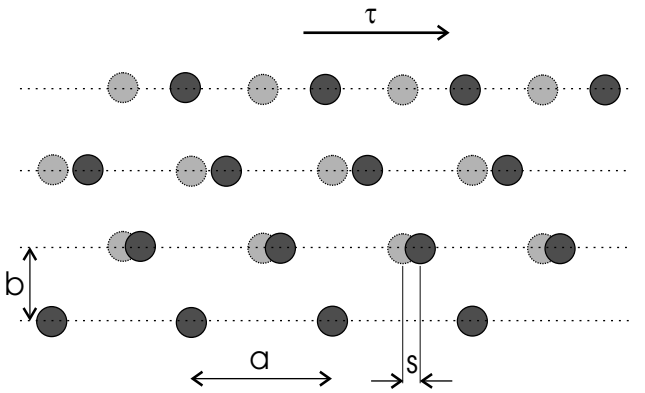

Figure 1.3 Scheme of the uniform shear applied to a perfect crystal

plane resulting in an atomically smooth fracture surface. Thus, the definition of IS as a maximum attainable stress along the deformation path was assigned to a stress related to the first onset of instability. Many stability studies were based on an analysis of the elastic response of crystals subjected to small homogeneous deformations. Such analyses of the mechanical stability, based on calculations of independent elastic moduli, led to a significant decrease in computed values of IS. This was the case for [001] uniaxial loading in Al, Nb and Cu [49, 67, 68]. More attention to this issue will be paid in Sections 1.1.2 and 1.1.3.

1.1.1.3 Other Advanced Methods

Besides *ab initio* approaches several other methods were also utilized for IS computations. Although these methods lie beyond the scope of this book, it is worthwhile making a brief comment on the topic.

In the last 20 years, very sophisticated semi-empirical methods such as many-body potentials of Finnis–Sinclair type [69], embedded atom method [69] or bond-order potentials [70] were used for analyses of extended crystal defects [71–73]. These concepts represent a hybrid between empirical and *ab initio* approaches. At present, the *ab initio* methods are only capable of giving a sufficiently precise prediction of the mechanical behaviour in very simple cases (but still far enough from the unstressed equilibrium state). This is the reason why, starting from the early 1990s, they are used for the calibration of semi-empirical potentials [42].

A further step towards identification of the initial onset of an instability was made by studies on the phonon spectra of crystal states along investigated deformation paths. This approach has further reduced the calculated values of IS [74]. The phonons are quasi particles used to express a particle aspect of lattice vibrations. They play a major role, e.g., in the theory of both

thermal and electric conductivity. However, they can also serve as an indicator of the lattice instability related to so-called soft phonon modes, at which the phonon frequency becomes an imaginary number. Such instabilities are responsible for various structural transitions [75,76] and, in general, they can be understood as an irreversible non-uniform (heterogeneous) distortion of a crystal. In this aspect, phonon analysis represents a generalization of elastic stability analysis since any observed elastic instability corresponds to a soft phonon mode with an infinite wavelength.

Once the crystal becomes unstable, it will follow a trajectory in a configurational space that will eventually violate the harmonic approximation inherent in the phonon calculation. In order to find such trajectories, molecular dynamic (MD) methods can be utilized. These approaches account for variations of the unit cell shape as well as the positions of constituent atoms. MD methods are probably the most promising tools for an investigation of the system stability and eventual structure evolutions during spontaneous structural transitions. They can give a sufficient number of degrees of freedom to studied systems and, furthermore, they can also incorporate finite temperatures and pressures thus bringing the simulations closer to reality. However, certain limitations related to computational capacity hinder them from wider applications. Present MD methods are mostly based on empirical or semi-empirical interatomic potentials. Some results obtained by means of these methods are mentioned in Section 1.2.

Let us finally note that the most sophisticated methods, including so-called correlated electron-ion dynamics, are even more computationally demanding. On the other hand, they may represent a reliable tool for atomistic simulations in the near future [77].

1.1.2 Calculation Principles

When applying atomistic approaches to a particular crystalline system, the dependence of its total energy on the deformation state constitutes the main output.

In order to describe the deformation of a crystalline system, it is necessary to define appropriate deformation parameters (strain variables). However, there is no unique way of defining a set of parameters which would provide a measure of a pure finite strain related to the crystal reference state. Therefore, one can find several different definitions used in the technical literature. A homogeneous strain of a crystal can be specified, e.g., by any six parameters that define a primitive cell. Some authors use lengths of cell edges (a_i) and their included angles (α_i) [66,78–80]. Although the deformation is described by changes of these parameters rather than themselves, they are also widely used in stability analyses. Such a natural set of variables is sometimes called Milstein's variables [79].

A simple description of any deformation that is used throughout this work employs a general rule on how to change position of an arbitrary point (e.g., atomic position) within the chosen coordinate system. This rule is expressed by a transformation matrix (deformation gradient) which is also called the Jacobian matrix J [81]. The practical advantage of such a description is apparent when one simulates a homogeneous deformation of a crystal through the deformation of its primitive cell. The primitive cell comprises both the motif and the set of vectors that determine the translational symmetry of a crystal. The transformation of vectors is then performed by multiplying by the Jacobian matrix.

Let us consider a crystalline system in a reference state with the corresponding set of primitive translational vectors $\mathbf{a_r}, \mathbf{b_r}, \mathbf{c_r}$. Applying a deformation described by J to the system, the set is transformed to a new set of vectors corresponding to the deformed state

$$\mathbf{a} = \mathsf{J}\mathbf{a_r}; \quad \mathbf{b} = \mathsf{J}\mathbf{b_r}; \quad \mathbf{c} = \mathsf{J}\mathbf{c_r}.$$

The tensor of a finite deformation (also called Lagrangian strain tensor) is defined according to the relation

$$\hat{\eta} = \frac{1}{2}(\mathsf{J}^T\mathsf{J} - \mathsf{I}),$$

where I means the identity matrix.

An equivalent definition of the finite strain tensor uses a rule that describes changes of lattice points positions via the displacement vector $\mathbf{u} = \mathbf{a} - \mathbf{a}_r$ and the matrix $e_{ij} = \partial u_i/\partial a_j$ [82]. When using the Einstein summation rule, the components of the finite strain tensor can then be written as

$$\eta_{ij} = \frac{1}{2}\left(\frac{\partial u_i}{\partial a_j} + \frac{\partial u_j}{\partial a_i} + \frac{\partial u_k}{\partial a_i}\frac{\partial u_k}{\partial a_j}\right). \tag{1.4}$$

The components η_{ii} refer to stretches and η_{ij} stands for shear strains if $i \neq j$.

A small deformation can also be depicted by a small strain tensor (known also as Euler strain, Green tensor or Cauchy infinitesimal strain):

$$\varepsilon_{ij} = \frac{1}{2}\left(\frac{\partial u_i}{\partial a_j} + \frac{\partial u_j}{\partial a_i}\right). \tag{1.5}$$

Hence, the finite strain differs from the small strain by the cross-term $\frac{\partial u_k}{\partial a_i}\frac{\partial u_k}{\partial a_j}$. Consequences of this difference with respect to the IS analysis are discussed in [83]. As the tensor represents a symmetric part of the matrix e_{ij}, any infinitesimal transformation can be expressed by a linear combination of the tensor ε_{ij} (describing pure deformation) and the antisymmetric part of the matrix e_{ij}

$$\omega_{ij} = \frac{1}{2}\left(\frac{\partial u_i}{\partial a_j} - \frac{\partial u_j}{\partial a_i}\right)$$

that represents the rotation as can be seen in Figure 1.4.

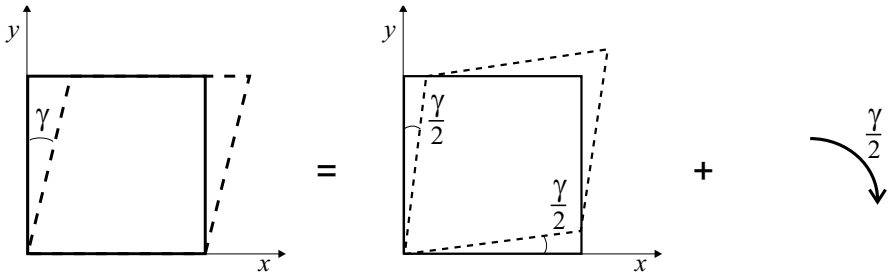

Figure 1.4 Two-dimensional illustration of lattice distortion (simple shear) as a pure shear plus a rotation $\hat{e} = \hat{\varepsilon} + \hat{\omega}$

As follows from Equations 1.4 and 1.5, both the strain tensors are symmetric (even if J is generally asymmetric). Therefore, it is useful to use Voigt notation that reduces the number of indices of symmetric tensors according to the prescription

$$\begin{array}{ll} 11 \to 1 & 23 \to 4 \\ 22 \to 2 & 13 \to 5 \\ 33 \to 3 & 12 \to 6. \end{array}$$

Thus, the second-rank tensor is reduced to a six-dimensional vector. Regrettably, there are two different standards used in the literature. The first one exactly follows the above-mentioned substitution $\eta_{ij} = \eta_\alpha$ (where indices i, j run from 1 to 3 and the index α runs from 1 to 6) [84,85] whereas the other one uses substitution $\eta_{ij} = \frac{1}{2}\eta_\alpha(1 + \delta_{ij})$ that leads to the following difference for the shear components: $\eta_4 = 2\eta_{23}$, $\eta_5 = 2\eta_{13}$ and $\eta_6 = 2\eta_{12}$ [82, 86–89]. The latter case is usually called standard Voigt notation. This simplifies the expression for energy expansion at Equation 1.7.

When a crystal system is subjected to a deformation, its energy changes (in the case of a stable state it increases, of course). The crystal energy can be expanded into Taylor series with respect to the finite strain η_{ij} as

$$U = U_0(V) + V\sigma_{ij}\eta_{ij} + \frac{1}{2}VC_{ijkl}\eta_{ij}\eta_{kl} + O(\eta^3), \tag{1.6}$$

where V represents a system volume, C_{ijkl} are elastic moduli and σ_{ij} are the related stress tensor components. In classical continuum mechanics, C_{ijkl} are usually called elastic constants [82]. However, the analysis of crystal stability (see Section 1.1.2.2) requires calculation of C_{ijkl} also at states far from equilibrium, where their values depend on the applied strain (or stress). In this book, therefore, the term *elastic moduli* is used for C_{ijkl}.

The symmetry of C_{ijkl} and σ_{ij} with respect to interchange of indices $(i \leftrightarrow j)$ and $(k \leftrightarrow l)$ enables us to use the Voigt notation for both of them.

The standard Voigt notation for strain $\eta_{ij} = \frac{1}{2}\eta_\alpha(1 + \delta_{ij})$ is used here. The corresponding energy expansion is then

$$U = U_0(V) + V\sigma_\alpha\eta_\alpha + \frac{1}{2}VC_{\alpha\beta}\eta_\alpha\eta_\beta + O(\eta^3). \tag{1.7}$$

Note that the energy expansion at Equation 1.7 contains a double sum instead of a quadruple sum in Equation 1.6.

1.1.2.1 Elastic Moduli

The 6×6 matrix of elastic moduli generally contains 21 independent elements that do not transform like the second-rank tensor components. According to the number of point group symmetry operations, the amount of independent elastic moduli can be lower. With respect to the energy expansion, the elastic moduli can be defined as

$$C_{\alpha\beta} = \frac{1}{V}\left(\frac{\partial^2 U}{\partial\eta_\alpha\partial\eta_\beta}\right)$$

or

$$c_{\alpha\beta} = \frac{1}{V}\left(\frac{\partial^2 U}{\partial\varepsilon_\alpha\partial\varepsilon_\beta}\right).$$

From now on, the C_{ij} will denote the elastic moduli defined on the basis of the finite strain and c_{ij} will stand for the elastic moduli based on the small strain.

When, for example, the crystal is subjected to small isotropic deformation, the lattice parameter a is related to the reference parameter a_r as $a = a_r(1 + e)$. Here e is a small stretch that represents diagonal components of the small strain tensor. Then, the finite strain is related to e according to $\eta_1 = \eta_2 = \eta_3 = \eta = e + \frac{e^2}{2}$, and the deformation gradient can be expressed as

$$\mathsf{J}_{iso} = \begin{pmatrix} 1+e & 0 & 0 \\ 0 & 1+e & 0 \\ 0 & 0 & 1+e \end{pmatrix} \quad \text{or} \quad \mathsf{J}_{iso} = \begin{pmatrix} \sqrt{1+2\eta} & 0 & 0 \\ 0 & \sqrt{1+2\eta} & 0 \\ 0 & 0 & \sqrt{1+2\eta} \end{pmatrix}.$$

The corresponding energy expansion at Equation 1.7 gives

$$U = U_0(V_r) + 3V_r\sigma\eta + \frac{1}{2}V_r(3C_{11}\eta^2 + 6C_{12}\eta^2) + \ldots$$

from which the following combination of elastic moduli:

$$C_{11} + 2C_{12} = \frac{1}{3V_r}\frac{\mathrm{d}^2 U}{\mathrm{d}\eta^2}$$

can be derived. Thus, this combination defines the bulk modulus

$$B = \frac{1}{3}(C_{11} + 2C_{12})$$

which expresses the elastic response of a crystal to isotropic (hydrostatic) loading.

Several other elastic moduli can be related to simple types of loading. For example, the modulus C_{11} can be determined by a simple lattice stretch in the [100] direction (see Figure 1.5). The Young's modulus expresses the crystal response to uniaxial loading and, therefore, it depends on the crystal orientation with respect to the loading direction. For particular orientations one can derive

$$E_{\langle 100\rangle} = \frac{(C_{11} - C_{12})(C_{11} + 2C_{12})}{C_{11} + C_{12}}, \tag{1.8}$$

$$E_{\langle 110\rangle} = 4\frac{C_{44}}{C_{11}}\left[1 + \frac{2C_{44}}{(C_{11} - C_{12})(C_{11} + 2C_{12})}\right]^{-1},$$

$$E_{\langle 111\rangle} = \frac{3C_{44}(C_{11} + 2C_{12})}{C_{44} + C_{11} + 2C_{12}}.$$

The shear modulus G can be expressed as

$$G = \frac{3C_{44}(C_{11} - C_{12})}{4C_{44} + C_{11} - C_{12}}$$

for $\{111\}\langle\bar{2}11\rangle$, $\{111\}\langle\bar{1}10\rangle$ and $\{110\}\langle\bar{1}11\rangle$ slip systems,

$$G = \frac{1}{2}(C_{11} - C_{12})$$

for $\{110\}\langle\bar{1}10\rangle$ slip system and $G = C_{44}$ for $\{110\}\langle001\rangle$ slip system.

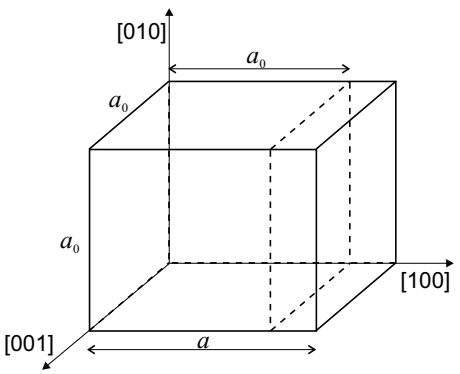

Figure 1.5 Illustration of a lattice distortion for calculation of the elastic modulus C_{11}

1.1.2.2 Mechanical Stability

Hereafter, the crystal potential energy U is determined from the electronic structure as E_{tot}. Thus, by using the internal energy per unit volume $E_u = E_{tot}/V$, one can also write

$$C_{ij} = \frac{\partial^2 E_u}{\partial \eta_i \partial \eta_j}$$

and

$$\sigma_i = \frac{\partial E_u}{\partial \eta_i}. \tag{1.9}$$

When no other instability (unstable phonon modes, phase transformations, elastic shear instabilities, etc.) occurs in the crystal, the relation at Equation 1.9 shows that IS corresponds to the first point of inflection on the energy *vs* strain curve ($C_{ij} = 0, \sigma_i = \sigma_{imax}$).

Probably the first attempt to formulate general criteria of crystal stability based on its elastic moduli was made in 1940 in the work of Born [64] and Born and Fürth [65]. They showed that by expanding the internal energy of a crystal in a power series in the strain and requiring positivity of the energy, one obtains a set of conditions on the elastic constants appropriate to the crystal that must be satisfied to maintain structural stability. It can be briefly said that, in the Born criterion, the system is stable if the matrix of elastic moduli C_{ij} is positive definite, i.e., all its eigenvalues are positive. Their results are valid only when the lattice is not under external stress.

In general, two basic cases of elastic (homogeneous) instability behaviour related to IS can be distinguished when analysing the crystal deformation:

1. instability occurs along the original deformation path,
2. instability changes the loading mode or the type of the deformation path.

The instability of the first kind (so-called volumetric instability) means that the process of unstable crystal collapse starts at the above-mentioned point of inflection on the original deformation path. Assuming the constant stress ensembles (i.e., the stress-controlled loading), the crystal starts to disintegrate spontaneously after reaching this point. During this process, however, strain induced phase transformations (so-called displacive transformations) may appear along the deformation path [90, 91]. These transformations proceed by means of cooperative displacements of atoms away from their lattice sites and alter the crystal symmetry without changing the atomic ordering or composition. They are of the first order and, therefore, accompanied by a symmetry-dictated extrema on the stress–strain curve. For example, the tetragonal Bain's path also induces typical displacive transformations (see Section 1.1.3). Moreover, additional extrema that are not dictated by the symmetry may occur, and reflect properties of the specific material. Consequently, more "IS values" can be found related to different points of inflection

on the energy–strain curve. However, the IS is determined by the stress associated with the first point of inflection on the original energy–strain curve which corresponds to the maximal energy gradient. Note that atomic configurations related to energy minima behind the first point of inflection may mimic stable or metastable atomic arrangements that could be encountered when investigating thin films or extended defects such as interfaces or dislocations. Similar configurations can also be reached during the strain-controlled deformation path of a crystal (the constant strain ensembles), provided that they are not preceded by any instabilities of the second kind.

The instabilities of the second kind (so-called shear instabilities) can be derived by considering a requirement that the free energy (and at $T = 0$ also the total internal energy) be minimum in subsequent constant stress ensembles in accordance with the second law of thermodynamics [66, 78–80, 87, 92–94]. The main point of such an analysis was the assumption that the crystal is subjected both to the applied load and to an infinite variety of small perturbing forces. Any of the forces can make the crystal fail in a different mode than that related to the main loading force. The proposed stability assessment requires information about an elastic response of the system to small deviations from the current state (let us call it the reference state). Therefore, in the case of a quasi-static loading, the stability assessment is in a sense independent of the deformation path which led the system to this state, because the same atomic arrangement can be obtained via many various transformations of an arbitrary original state. For that reason, the further deformations used to investigate the stability have nothing to do with the original deformation path. If the solid is strained infinitesimally from the reference state associated with the stress σ_{ij} (in the standard notation) by a strain tensor ε_{ij}, the related Cauchy (true) stress τ_{ij} can be written as

$$\tau_{ij} = \sigma_{ij} + B_{ijkl}\varepsilon_{kl},$$

where

$$B_{ijkl} = C_{ijkl} + \frac{1}{2}\left(\delta_{ik}\sigma_{jl} + \delta_{jk}\sigma_{il} + \delta_{il}\sigma_{jk} + \delta_{jl}\sigma_{ik} - 2\delta_{kl}\sigma_{ij}\right) \tag{1.10}$$

is the elastic stiffness matrix $(i, j, k, l = 1, 2, 3)$ introduced by Wallace [95] that is generally asymmetric with respect to the interchange of indices. Construction of this matrix is crucial for the stability assessment. As was shown in [92, 94, 96], the system becomes unstable once its symmetrized counterpart

$$\mathsf{A} = \frac{1}{2}\left(\mathsf{B}^T + \mathsf{B}\right)$$

attains a zero determinant, i.e.,

$$|\mathsf{A}| = 0 \tag{1.11}$$

during the loading. It should be emphasized that the elastic moduli in Equation 1.10 are the local ones, i.e., corresponding to different points of the deformation path. Thus, in order to assess the stability, their values should be determined by introducing a sufficient number of independent small deviations (strain increments) away from the original deformation path at each point, in accordance with the symmetry of the particular crystal lattice. The solution of Equation 1.11 gives a different number of possible stability conditions for different crystal lattice symmetries as well as different loading modes. The higher the symmetry (the more point group symmetry operations), the fewer the stability conditions are to be tested. The smallest possible number of necessary stability conditions (only two) corresponds to the isotropic solid.

The stability conditions for cubic crystals loaded in uniaxial tension or compression along the [001] direction, the so-called Bain's path, can serve as a suitable example. The tetragonal symmetry induced by the uniaxial loading means $C_{11} = C_{22} \neq 0, C_{33} \neq 0, C_{12} \neq 0, C_{13} = C_{23} \neq 0, C_{44} = C_{55} \neq 0, C_{66} \neq 0$ and $C_{ij} = 0$, other, and a simple relationship $\sigma_{ij} = \sigma\delta_{i3}\delta_{j3}$ stands for the stress tensor. By introducing these relations into Equation 1.11, one obtains the following stability conditions:

$$(C_{33} + \sigma)(C_{12} + C_{11}) - 2(C_{13} - \sigma/2)^2 > 0, \tag{1.12}$$

$$C_{11} - C_{12} > 0, \tag{1.13}$$

$$2C_{44} + \sigma > 0, \tag{1.14}$$

$$C_{66} > 0. \tag{1.15}$$

The left-hand side of Equation 1.12 differs from the tetragonal $E_{[001]}$ modulus for the stress-free state $\sigma = 0$ only by a multiplication constant. Therefore, the violation of that so-called volumetric condition is closely related to the first inflection point on the energy *vs* strain curve along the [001] deformation path (the instability of the first kind). In any case, the maximum value of the stress determining the IS along the [001] path is associated with the point of inflection. This is the main reason why the testing of the volumetric instability can actually be omitted. All the other conditions prevent the crystal from shear (second-kind) instabilities. Breaking the condition at Equation 1.13 causes a shear bifurcation from the tetragonal deformation path to the orthorhombic one [46, 85]. In the case of the fcc crystal, this instability induces branching to the tetragonal face centred orthorhombic path – it is the so-called Born's instability. The instabilities at Equations 1.14 and 1.15 are related to C_{44} and C_{66} shear moduli, respectively.

In order to test the shear-related criteria, special local Lagrangian deformations (determined by corresponding Jacobi matrices) are to be applied to

the crystal at each point of the deformation path. For the tetragonal path [68], the Jacobi matrix

$$\mathsf{J}_{C'} = \begin{pmatrix} \sqrt{1+2e} & 0 & 0 \\ 0 & \sqrt{1-2e} & 0 \\ 0 & 0 & 1 \end{pmatrix}$$

and the corresponding deformation matrix

$$\hat{\eta}_{C'} = \begin{pmatrix} e & 0 & 0 \\ 0 & -e & 0 \\ 0 & 0 & 0 \end{pmatrix}$$

lead to the following change of the system energy (per volume unit) according to Equation 1.7:

$$\Delta E_u = (C_{11} - C_{12})e^2 + \dots$$

This deformation changes the tetragonal symmetry to the orthorhombic one but the calculated $\Delta E_u(e)$ curve is symmetric ($\Delta E_u(e) = \Delta E_u(-e)$). With regard to the energy expansion, the tetragonal shear modulus $C' = 0.5(C_{11} - C_{12})$ can be expressed as

$$C' = \frac{1}{4}\frac{\partial^2 \Delta E_u}{\partial e^2}.$$

The condition at Equation 1.14 corresponds to the shear instability related to the C_{44} modulus. Using the Jacobi matrix and strain as

$$\mathsf{J}_{C_{44}} = \begin{pmatrix} 1 & 0 & 0 \\ 0 & \dfrac{\sqrt{1+2e}+\sqrt{1-2e}}{2} & \dfrac{2e}{\sqrt{1+2e}+\sqrt{1-2e}} \\ 0 & \dfrac{2e}{\sqrt{1+2e}+\sqrt{1-2e}} & \dfrac{\sqrt{1+2e}+\sqrt{1-2e}}{2} \end{pmatrix}, \quad \hat{\eta}_{C_{44}} = \begin{pmatrix} 0 & 0 & 0 \\ 0 & 0 & e \\ 0 & e & 0 \end{pmatrix},$$

one obtains the dependence $\Delta E_u(e)$ leading to

$$\Delta E_u = 2C_{44}e^2 + \dots$$

and

$$C_{44} = \frac{1}{4}\frac{\partial^2 \Delta E_u}{\partial e^2}.$$

The stability condition at Equation 1.15 can be tested by using

$$\mathsf{J}_{C_{66}} = \begin{pmatrix} \dfrac{\sqrt{1+2e}+\sqrt{1-2e}}{2} & \dfrac{2e}{\sqrt{1+2e}+\sqrt{1-2e}} & 0 \\ \dfrac{2e}{\sqrt{1+2e}+\sqrt{1-2e}} & \dfrac{\sqrt{1+2e}+\sqrt{1-2e}}{2} & 0 \\ 0 & 0 & 1 \end{pmatrix}, \quad \hat{\eta}_{C_{66}} = \begin{pmatrix} 0 & e & 0 \\ e & 0 & 0 \\ 0 & 0 & 0 \end{pmatrix}.$$

The corresponding energy change reads

$$\Delta E_u = 2C_{66}e^2 + \ldots$$

and the modulus

$$C_{66} = \frac{1}{4}\frac{\partial^2 \Delta E_u}{\partial e^2}.$$

Let us also show the stability conditions applied for a cubic structure (with 48 symmetry operations) under isotropic loading ($\sigma_1 = \sigma_2 = \sigma_3 = \sigma$). Here the form of the Wallace matrix (Equation 1.10) becomes symmetric:

$$\mathsf{B} = \begin{pmatrix} C_{11}+\sigma & C_{12}-\sigma & C_{12}-\sigma & 0 & 0 & 0 \\ C_{12}-\sigma & C_{11}+\sigma & C_{12}-\sigma & 0 & 0 & 0 \\ C_{12}-\sigma & C_{12}-\sigma & C_{11}+\sigma & 0 & 0 & 0 \\ 0 & 0 & 0 & C_{44}+\sigma & 0 & 0 \\ 0 & 0 & 0 & 0 & C_{44}+\sigma & 0 \\ 0 & 0 & 0 & 0 & 0 & C_{44}+\sigma \end{pmatrix}$$

and its determinant

$$\det|\mathsf{B}| = (C_{44}+\sigma)^3(C_{11}-C_{12}+2\sigma)^2(C_{11}+2C_{12}-\sigma)$$

can be broken down into to a set of stability conditions:

$$\begin{aligned} &1. \quad C_{11}+2C_{12}-\sigma > 0 \\ &2. \quad C_{11}-C_{12}+2\sigma > 0 \\ &3. \quad C_{44}+\sigma > 0. \end{aligned} \tag{1.16}$$

Stability criteria for a tetragonal system under biaxial (epitaxial) loading as well as those for the simplest case of an isotropic solid under hydrostatic loading can be found elsewhere [83].

Let us recall that, in addition to the violation of the mechanical stability conditions, some phonon (heterogeneous) instabilities may occur along the deformation path. A more detailed description of this problem lies beyond the scope of this book.

The currently used methodology for the IS calculation can be, finally, briefly summarized in the following points:

1. construction of a suitable empirical interatomic potential or calculation of the electronic structure;
2. calculation of the energy–strain curve and the related stress *vs* strain dependence for a specific deformation path;
3. establishment of elastic and phonon instability ranges on the strain *vs* energy and/or stress *vs* strain curves;
4. determination of IS value as a stress related to the first instability point on the energy *vs* strain curve.

1.1.3 Simple Loading Modes

1.1.3.1 Ideal Isotropic Strength

A nearly isotropic, triaxial tensile stress state ($\sigma_1 = \sigma_2 \approx 1.6\sigma_3$) builds up at the tip of cracks in solids stressed by uniaxial tension (e.g., [8]). The value of σ_{iht} expresses a resistance to a brittle fracture (cleavage or tearing at a sharp crack tip), while the value of τ_{is} reflects a defiance to a ductile response (blunting of the crack tip). Consequently, the ratio σ_{iht}/τ_{is} can be used as a measure of the brittle/ductile behaviour of cracked perfect crystals [23–25] (see also Section 1.2). This is why the search for isotropic IS values also becomes worthwhile from the engineering point of view. To our best knowledge, however, there are no available experimental data on σ_{iht}. The reason lies in difficulties in experimental realization of an isotropic tensile loading. Thus, a theoretical assessment remains to be the only applicable tool to gain such information. When the isotropic deformation is applied to a system, its volume changes but the symmetry remains unchanged (unless a phase transition takes place). Under such conditions, a rather simple LMTO-ASA method is particularly suitable for *ab initio* calculations (see Appendix A). Indeed, the error of ASA approximation is nearly independent of the volume.

Let us consider a cubic crystal under applied isotropic stress σ. A natural parameter for a description of deformation is the crystal volume V. The deviation from the equilibrium (unstressed) volume V_0 can be expressed by the relative (normalized) volume $v = V/V_0$. The isotropic stress can be simply derived from the dependence of the crystal energy U (see Figure 1.6) on the relative volume v as

$$\sigma_{iht} = \frac{1}{V_0}\frac{\mathrm{d}U}{\mathrm{d}v}.$$

The stress σ_{iht} reaches its maximum value when

$$\frac{\mathrm{d}^2U}{\mathrm{d}v^2} = 0, \tag{1.17}$$

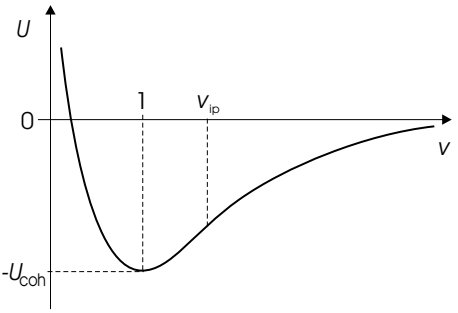

Figure 1.6 A schematic dependence of the crystal potential energy U on the relative volume v. The region with $v < 1$ corresponds to compression, $v > 1$ to tension and v_{ip} is assigned to the point of inflection. U_{coh} represents the cohesive energy of a crystal when a zero energy is related to a system of isolated atoms ($\lim_{v\to\infty} U = 0$)

Table 1.1 Theoretical isotropic strength σ_{iht} from *ab initio* and semi-empirical approximations

Element		Theoretical strength σ_{iht} (GPa)							
		ab initio results				Semi-empirical results			
		LMTO		VASP		Polynomial	Morse	Sinus	DVC
		[97]	[97]	[98]	[99]	[36]	[36]	[36]	[100]
Li	bcc	3.53[a]	3.13[b]			5.06	2.49	4.91	1.92
C	dia	66.1[a]	53.2[b]	88.5[a]	88.5[a]	84.7	69.7	138	
Na	bcc	1.97[a]	1.55[b]			1.87	1.20	1.86	1.77
Al	fcc	13.8[a]	12.0[b]		11.2[b]	22.2	11.9	23.0	
Si	dia	15.0[a]	10.4[b]	15.5[a]	15.4[a]	15.1	13.7	28.2	
K	bcc	0.955[a]	0.701[b]			0.99	0.659	1.28	0.10
V	bcc	39.2[a]	33.2[b]	32.7[b]		32.6	23.5	45.4	38.3
Cr	bcc	37.2[a]	21.0[b]			35.2	25.9	50.2	47.4
Fe	bcc	37.7[a]	26.7[b]	27.7[b]	28.5[b]	33.8	24.1	48.1	
Ni	fcc	39.5[a]	27.4[b]	28.9[b]	29.2[b]	44.7	26.9	51.2	
Cu	fcc	28.8[a]	20.9[b]	19.8[b]	20.4[b]	32.7	19.9	38.4	
Ge	dia	11.0[a]	6.46[b]	11.1[a]		11.3	10.1	21.4	
Nb	bcc	36.3[a]	31.6[b]	31.6[b]		35.5	25.5	49.4	34.1
Mo	bcc	49.3[a]	42.7[b]	42.9[b]	43.2[b]	48.2	35.0	68.9	42.2
Ag	fcc	19.0[a]	12.6[b]		17.6[a]	20.2	13.7	26.7	
Ba	bcc	2.69[a]	1.93[b]			2.36	1.64	3.17	
Ta	bcc	41.3[a]	36.4[b]			39.2	28.5	55.1	41.3
W	bcc	57.0[a]	50.6[b]	50.7[b]	50.2[b]	56.1	42.2	80.1	53.1
Ir	fcc			40.1[b]		61.2	45.6	85.6	
Pt	fcc	42.7[a]	33.6[b]	39.6[a]		48.5	35.1	68.0	
Au	fcc	25.5[a]	17.6[b]	23.2[a]	23.5[a]	28.4	20.9	39.9	
Pb	fcc	8.7[a]	6.98[b]			7.91	5.47	10.6	

[a] LDA
[b] GGA

i.e., at the inflection point of the $U(v)$ dependence ($v \to v_{ip}$). Considering the bulk modulus as a parameter expressing the elastic response of the crystal to the volume change as

$$B = \frac{\mathrm{d}\sigma_{iht}}{\mathrm{d}v} = \frac{1}{V_0}\frac{\mathrm{d}^2 U}{\mathrm{d}v^2}, \tag{1.18}$$

the volume at which the equality at Equation 1.17 is valid corresponds to vanishing of the bulk modulus. In other words, the first (volumetric) condition of a stability set at Equation 1.16 related to the isotropic loading of cubic crystals is fulfilled. Indeed, the bulk modulus is defined by the combination $C_{11} + 2C_{12}$ of elastic constants. In the further analysis, the crystal potential energy U will be substituted by a total energy E_{tot} that is evaluated from the electronic structure of investigated crystals. Thus, the first stability condition is related to the inflection point of the dependence of the total energy on the volume. The violation of the second stability condition corresponds to a shear instability (vanishing of the tetragonal shear modulus) when we can expect a bifurcation from the primary deformation (isotropic) path to a secondary one, where the lattice acquires tetragonal or orthorhombic symmetry. The third condition corresponds to another shear instability related to the trigonal shear modulus.

The values of σ_{iht} for various cubic crystals, as determined by *ab initio* approaches, are reported in our papers [60–62] and displayed in Table 1.1. The stability analysis, performed for crystals of Cu, Al, Ag, Fe, Ni and Cr, revealed that all these crystals fail under the volumetric instability [62]. This means that the values of the stress related to the point of inflection really correspond to σ_{iht}. The associated relative change of volume is about 1.5, which means that the relative elongation of the lattice parameter is about 1.15. In the case of aluminium crystal, however, the *ab initio* approach indicated a break in the trigonal shear stability before reaching the inflection point. Because this is in disagreement with results achieved by several other authors [80, 94], the problem of the aluminium crystal is open for further investigations. For a majority of crystals, nevertheless, the values of σ_{iht} are higher than τ_{is} and σ_{iut}. Indeed, the values of τ_{is} are generally much lower since, to reach this value, the atoms in the shear plane need not be separated by higher distances. During uniaxial tension, the shear instabilities appear well before reaching σ_{iut} at the inflection point (see next subsections).

Table 1.2 Theoretical and experimental ideal strength data

Crystal	Ideal strength [GPa]													
	Isotropic		Uniaxial						Shear					
	σ_{iht}	Ref.	σ_{iut}	Direct.	Ref.	$\sigma_{\exp}$	Direct.	Ref.	τ_{is}	Direct.	Ref.	$\tau_{\exp}$	Direct.	Ref.
Al (fcc)	11.0	[62]	9.2	⟨100⟩	[101]	2.27	bending	[33]	2.84	⟨112⟩	[99]			
			9.0	⟨111⟩	[101]				2.94	⟨112⟩	[59]			
			4.9	⟨110⟩	[101]				1.85	⟨112⟩	[85]			
			9.0	⟨100⟩	[102]				3.07	⟨112⟩	[102]			
			8.8	⟨111⟩	[102]				3.77	⟨110⟩	[103]			
			4.5	⟨110⟩	[102]									
Cu (fcc)	20.2	[62]	9.4	⟨001⟩	[68]	1.74	⟨001⟩	[33]	2.38	⟨112⟩	[59]	0.61	⟨011⟩	[30]
			9.3	⟨001⟩	[102]	1.59	⟨110⟩	[33]	3.77[b]	⟨011⟩	[103]			
			4.5	⟨110⟩	[102]	1.25	⟨111⟩	[30]						
			7.5	⟨111⟩	[102]	2.94	⟨111⟩	[33]						
Ni (fcc)	27.4	[61]	18.3	⟨001⟩	[102]				5.02	⟨112⟩	[59]			
			9.1	⟨110⟩	[102]				5.05	⟨112⟩	[99]			
			15.4	⟨111⟩	[102]									
Ag (fcc)	11.4	[62]				3.80	⟨001⟩	[30]	1.65	⟨112⟩	[99]	0.71	⟨011⟩	[30]
						1.73	⟨001⟩	[33]						
Au (fcc)	17.6	[97]							0.85	⟨112⟩	[99]			
									1.06	⟨112⟩	[59]			

[a]Inflection point
[b]Unrelaxed
[c]Semi-empirical

Table 1.2 (continued)

Crystal	Ideal strength [GPa]													
	Isotropic		Uniaxial						Shear					
	σ_{iht}	Ref.	σ_{iut}	Direct.	Ref.	$\sigma_{\exp}$	Direct.	Ref.	τ_{is}	Direct.	Ref.	$\tau_{\exp}$	Direct.	Ref.
Na (bcc)	1.77	[63]							0.20	⟨112⟩{111}	[85]			
	2.18	[104]												
Fe (bcc)	26.7	[61]	14.2	⟨001⟩	[101]	13.1	⟨111⟩	[30]	7.51	⟨111⟩{112}	[99]	3.56	⟨111⟩{110}	[30]
			27.3[a]	⟨111⟩	[43]				8.14	⟨111⟩{110}	[99]			
Mo (bcc)	42.7	[97]	28.8[a]	⟨001⟩	[49]				15.18	⟨111⟩{110}	[99]			
									14.84	⟨111⟩{211}	[99]			
W (bcc)	53.1	[63]	28.9[a]	⟨001⟩	[41]	24.7	⟨001⟩	[23]	17.52	⟨111⟩{110}	[99]			
	57.4	[60]	40.1[a]	⟨111⟩	[41]				17.37	⟨111⟩{211}	[99]			
	50.6	[97]	54.3[a]	⟨110⟩	[41]									
			29.5[a]	⟨001⟩	[57]									
Cr (bcc)	21.0	[61]							20.5	⟨111⟩{112}	[105]			
Zn (hcp)									2.12	⟨111⟩{112}	[99]			
C (diam)			90.0[a]	⟨111⟩	[47]	20.7	(hex)	[30]	113.32	⟨110⟩{111}	[99]			
			95.0[a]	⟨111⟩	[48]	19.6	(hex)	[33]	99.60	⟨112⟩{111}	[106]			
			130.0[a]	⟨100⟩	[47]				93.0	⟨112⟩{111}	[48]			

[a]Inflection point
[b]Unrelaxed
[c]Semi-empirical

Table 1.2 (continued)

Crystal	Ideal strength [GPa]													
	Isotropic		Uniaxial						Shear					
	σ_{iht}	Ref.	σ_{iut}	Direct.	Ref.	$\sigma_{\exp}$	Direct.	Ref.	τ_{is}	Direct.	Ref.	$\tau_{\exp}$	Direct.	Ref.
Ge (diam)			14.0[a]	⟨111⟩	[48]	3.82	(bend)	[33]	5.4	⟨112⟩{111}	[106]			
									4.3	⟨112⟩{111}	[48]			
Si (diam)	26.4	[60]	22.0[a]	⟨111⟩	[48]	7.60	(bend)	[33]	8.6	⟨112⟩{111}	[106]			
									6.8	⟨112⟩{111}	[48]			
Ni_3Al ($L1_2$)	28.1	[107]	17.5[a]	⟨100⟩	[108]									
			28.2[a]	⟨111⟩	[108]									
NiAl (B2)	25.6	[107]	46.0[a]	⟨001⟩	[109]									
			25.0[a]	⟨111⟩	[109]									
SiC (B3)			101.0[a]	⟨001⟩	[46]				31.74	⟨110⟩{111}	[99]			
			50.8[a]	⟨111⟩	[46]									
MgO (B1)	38.5[c]	[36]	37.0[c]	⟨100⟩	[36]	23.7	(bend)	[33]	17.09	⟨110⟩{110}	[99]			
Si_3N_4			55.0[a]	⟨100⟩	[83]	13.5		[33]	19	⟨0001⟩{1010}	[99]			

[a]Inflection point
[b]Unrelaxed
[c]Semi-empirical

It is to be expected that the values of σ_{ihc} could even be much higher than those of σ_{iht}. This was confirmed by a stability analysis of Ni, Cr and Fe crystals [58]. No instability was found in the compressive region up to 50% of unstressed volume V_0 in the cases of Ni and Cr which means that the values of σ_{ihc} must be, at least, several hundred GPa. The stress corresponding to the break of the third stability condition in Fe is 200 GPa. This is in agreement with previously predicted instability of bcc iron under pressure [110], at which the tetragonal meta-stable phase develops. As has been experimentally observed, however, that the bcc $\rightarrow$ hcp phase transition already starts at pressures of about 10–15 GPa [111]. This implies that this kind of instability cannot be revealed by mechanical stability analysis and, therefore, an identification of phonon instability ranges might be more helpful. However, we are not aware of any studies of this kind.

1.1.3.2 Ideal Tensile Strength

When a uniaxial tensile stress is applied to any cubic crystal, its symmetry becomes reduced. In the case of [001] loading, the crystal acquires a tetragonal symmetry with 16 symmetry operations. A model of two adjacent elementary fcc cells subjected to [001] loading is displayed in Figure 1.7.

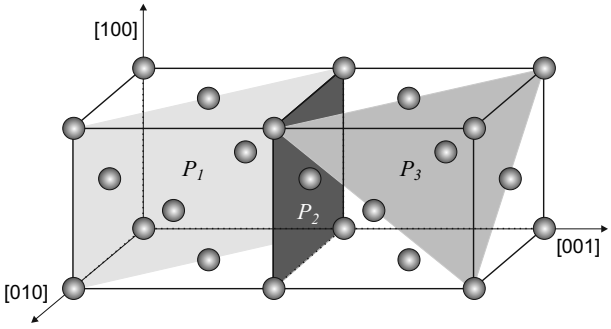

Figure 1.7 Illustration of fcc lattice extended in [001] direction with examples of one tear plane (P_2) and two possible shear (P_1 and P_3) planes

Experiments on whiskers [1,33] suggested that, under such particular loading, the lattice usually fails by the shear in the {111} plane (P_3 in Figure 1.7) in fcc systems or in the {110} plane (P_1 in Figure 1.7) in bcc systems rather than by the tear along the {001} plane (P_2 in Figure 1.7) – see also Section 1.1.4.3. The latter fracture process was assumed not only in the very first calculations of tensile strength [1] but even in a majority of later studies (e.g., [39, 41, 74, 112]). The elastic matrix of the tetragonal system contains six independent components:

$$\mathsf{C} = \begin{pmatrix} C_{11} & C_{12} & C_{13} & 0 & 0 & 0 \\ C_{12} & C_{11} & C_{13} & 0 & 0 & 0 \\ C_{13} & C_{13} & C_{33} & 0 & 0 & 0 \\ 0 & 0 & 0 & C_{44} & 0 & 0 \\ 0 & 0 & 0 & 0 & C_{44} & 0 \\ 0 & 0 & 0 & 0 & 0 & C_{66} \end{pmatrix}$$

and the corresponding stability analysis is presented in [68, 78, 113], particularly in Section 1.1.2. For example, the copper crystal was found to fail in shear at the tensile stress of 9.4 GPa, well before the volumetric instability at 24.3 GPa. This result is in good agreement with the calculations of Milstein and Chantasiriwan [78]. Unfortunately, practically all the previously calculated σ_{iut} values of different crystals are related to the volumetric instability (see Table 1.2) and, therefore, they substantially exceed the real ones. Moreover, the older studies did not include the atomic relaxation procedures enabling the transverse Poisson's contraction. Nevertheless, a mutual comparison of those values can serve as an orientation ordering of various crystals according to their uniaxial IS.

As can be seen in Table 1.2, there is a three-order of magnitude difference between the strongest and the weakest crystal. As expected, the highest IS value belongs to the diamond crystal with pure covalent bonds and the lowest values to the Van der Waals crystals of inert gases that are stable only in the low temperature range. High values of σ_{iut} of metals as W, Mo and Fe or intermetallics such as Ni_3Al and AlN are also understandable due to a high portion of covalent interatomic bonds in these crystals. It should be emphasized that this ranking of σ_{iut} is, more or less, compatible with that of ultimate strength σ_u for real crystals and engineering materials. This means that the intrinsic (matrix) strength properties predetermine the ultimate strength of the engineering materials in a rather significant manner.

1.1.3.3 Ideal Shear Strength

Unlike tensile and compressive deformation modes, the pure shear deformation process does not require any elastic stability assessments because it is expected to maintain, more or less, the original shear path. On the other hand, the symmetry of the crystal lattice is almost disturbed by the shear shifts and, therefore, the calculation procedures become rather cumbersome. Moreover, the full relaxation of atomic positions near the shear plane, allowing them to follow configurations of lowest total crystal energies along the whole shear trajectory, are essential for obtaining sufficiently precise values of τ_{is} [49, 99, 103].

A great majority of analyses published before the year 2000 did not utilize the relaxation procedure. From all these results let us mention only a rather general study made on fcc, bcc, diamond, B1 and B2 structures. In this study, the block-like shear was simulated by using both central and non-

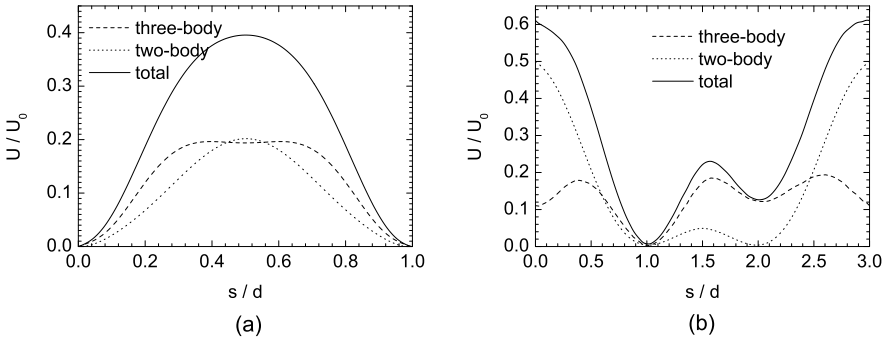

Figure 1.8 Shear potentials in the slip system (a) $\{111\}\langle 110\rangle$, (b) $\{111\}\langle 112\rangle$, non-central forces. U_0 is energy at the equilibrium (unstressed) position in utilized semi-empirical potentials

central empirical potentials [31]. Shapes of the potential energy along shear trajectories in fcc crystallographic systems $\langle\bar{1}10\rangle\{111\}$ and $\langle\bar{2}11\rangle\{111\}$, as computed using non-central potentials, are displayed in Figure 1.8. It can be seen that, in spite of the shallow local minimum created by the large non-central component (three-body), the total energy shape in Figure 1.8(a) is of a sinusoidal type, as originally presumed by Frenkel. Another investigated shear system in Figure 1.8(b) exhibits a secondary energy minimum that is related to the stable stacking fault. These results are in contradiction to the already mentioned Mackenzie theory that assumes an existence of a shallow minimum on the total energy curve in the range $s/d \in (1, 2)$. This is one of the main reasons why the calculated values of τ_{is} approach those already reported by Frenkel (see Table 1.3).

Table 1.3 Ideal strength in simple shear direction (a is the lattice parameter)

Lattice	Direction	Plane	d/a	b/a	τ_{id}/G
bcc	$\langle 111\rangle$	$\{110\}$	$\sqrt{3}/2$	$1/\sqrt{2}$	0.1949
fcc	$\langle 110\rangle$	$\{111\}$	$1/\sqrt{2}$	$1/\sqrt{3}$	0.1949
fcc	$\langle 112\rangle$	$\{111\}$	$1/\sqrt{6}$	$1/\sqrt{3}$	0.1025
B1	$\langle 110\rangle$	$\{110\}$	$1/\sqrt{2}$	$1/\sqrt{8}$	0.3183
B2	$\langle 001\rangle$	$\{110\}$	1	$1/\sqrt{2}$	0.2251
diam	$\langle 110\rangle$	$\{111\}$	$1/\sqrt{2}$	$\sqrt{3}/4$	0.2599

In most *ab initio* studies, a uniform shear of a perfect crystal was simulated, as is schematically depicted in Figure 1.3. Moreover, the first principles codes enable minimization of all stress tensor components, except for the resolved shear stress, to approximately zero values by appropriate shifting of atoms not only in the direction perpendicular to the shear plane, but also

within this plane (so-called in-plane relaxation). This can be done by using the procedure based on the Hellman–Feynman forces, which is part of some *ab initio* program codes (VASP, Abinit). Consequently, the resulting (optimal) shear trajectory is usually slightly different from that prescribed by crystallography.

1.1.3.4 Comparison of Theoretical and Experimental Results

Because of the long history of IS calculations, a number of theoretical results concerning crystals of pure elements and compounds are available in the literature. On the other hand, the experimental data are rather limited which is related to problems associated with both specimen preparation and experimental arrangement. It is particularly difficult to measure the values of σ_{iht} and τ_{is}, although, for measuring the latter, nanoindentation appears as a good tool today (see Section 1.3).

Theoretical and experimental values of σ_{iht}, σ_{iut} and τ_{is} for various crystals are presented in Table 1.2. The lowest values of σ_{iut} for a particular crystal have always been found in calculations with full relaxations that also take the mechanical stability conditions into account. It can be seen that theoretical and experimental values can differ substantially according to the applied computational or experimental procedure. Nevertheless, the *ab initio* methods can be considered as the most reliable ones. It should be emphasized that a majority of σ_{iut} values correspond to the inflection point of the energy *vs* strain curve when omitting the stability analysis. Hence, most of such calculated values are substantially overestimated.

Rather rare experiments provided τ_{is} values of about 2–3 times lower than those calculated by means of the *ab initio* methods. Older experimental data on τ_{is} were obtained by recalculating the results of uniaxial tensile testing of whiskers by omitting the influence of the normal stress component (see Section 1.1.4 for more details). When taking this influence into account, the maximum resolved shear stresses at fracture are still substantially lower than the theoretical ones, but already of the same order of magnitude. Note that the most sophisticated methods based on nanoindentation tests render data almost in accordance with the recent theory (see Section 1.3 for more details). This is a very encouraging message showing that, at least in the case of τ_{is}, the advanced theoretical and experimental methods start to agree.

In the case of metals, a majority of experimental σ_{iut} data obtained on perfect large single crystals or whiskers are of an order of magnitude lower than those calculated even by means of *ab initio* methods considering the mechanical or phonon shear instabilities. This might be due to the dislocation-assisted shear instability controlling the final failure process. On the other hand, a very high Peierls–Nabarro stress in covalent and complex ionic ceramic crystals resists the nucleation and motion of dislocations. Indeed, for such crystals the difference between theory and experiment is relatively small. Probably the

highest ever reported experimental value $\sigma_{iut} = 40\,\mathrm{GPa}$ ($\approx E/20$) is for the ZnO whiskers [33]. However, experiments performed on tungsten whiskers by Mikhailovskii *et al.* [114] also approach the calculated results. Anyway, the discrepancy between theory and experiment for metallic crystals becomes much smaller when the mechanical and phonon stability conditions are taken into account (e.g., for Cu [68] and Al [101] crystals), though it still remains significant. It should be noted that the stability conditions imply that the loading mechanism should be able to maintain the Cauchy stress and the crystal symmetry along the whole deformation path. It particularly means that the shear instability $\langle\bar{2}11\rangle\{111\}$ in the case of [001] tension of the fcc crystal is not controlled by the stability conditions, although it is a usually observed failure mode in experiments. Indeed, this instability requires a finite shear in the $\{111\}$ plane changing the symmetry to triclinic or monoclinic. Additionally, a possible resonance of short-wavelength phonons should be considered. Such effects are clearly beyond the description supplied by the mechanical stability conditions that are based only on continuum mechanics. Nevertheless, the difference between theory and experiment can be understood particularly in terms of various imperfections of experimental procedure and the crystal defects.

Anyway, a lot of work is needed in both theoretical and experimental investigations of IS. Let us finally note that the ultimate strength of currently used ultra-high-strength steels still exhibits only a rather small fraction of the IS of the iron crystal. From the theoretical point of view, however, materials of an extreme dislocation density could, in principle, achieve more than half of the strength level of σ_{iut} [20]. This also holds for amorphous solids.

1.1.4 Multiaxial Loading

Although there is no doubt that crystals and whiskers used in industrial exploitation are usually subjected to multiaxial loading, little attention has been paid to the coupling of various stress tensor components. Another example of the practical importance is associated with reinforcing fibres used in engineering composite materials. Due to the matrix/reinforcement incompatibility strains, the single crystal fibres (or whiskers) are subjected to multiaxial loading even in the case of remote uniaxial tension of the composite. Consequently, *ab initio* modelling of the uniaxial tension of perfect crystals under superimposed tensile or compressive biaxial stresses is expected to be a reasonable theoretical simulation of the stress-strain behaviour of composite fibres (see Section 1.1.5). Several studies were also focused on the influence of superimposed hydrostatic or normal stress on the shear IS [103, 115, 116]. The results reveal, as a rule, an increase in the shear strength with increasing compressive normal stress. Such analyses allow us, for example, to predict the very onset of plastic deformation under the nanoindenter (see Section 1.3).

1.1.4.1 Coupling of Uniaxial and Transverse Biaxial Stresses

In order to describe the influence of superimposed transversal biaxial stress on the tensile IS of metallic fibres in composites, bulk systems of several metallic and covalent ideal crystals subjected to multiaxial loading were studied in [117]. The calculation procedure based on the VASP code was applied to ten cubic crystals (V, Fe, Ni, Cu, Nb, Mo, W, Ir, Pt and Au) and three crystals of a diamond structure (C, Si and Ge). All studied crystalline systems were subjected to the uniaxial tensile stress σ_{uni} along [100] direction combined with the transverse biaxial stress σ_{bi} in the (100) plane (see Figure 1.9). A relaxation procedure based on the Hellman–Feynman forces in (100) plane was applied in order to get the stress tensor in a simple form as

$$\hat{\sigma} = \begin{pmatrix} \sigma_{uni} & 0 & 0 \\ 0 & \sigma_{bi} & 0 \\ 0 & 0 & \sigma_{bi} \end{pmatrix}.$$

The relaxation process consisted of the following steps:

1. The crystal was subjected to σ_{bi} of a certain preset value.
2. The crystal was incrementally elongated in the [100] direction and the value of σ_{bi} was converged to the same preset value for any elongation.
3. The stress maximum $\sigma_{\max}$ and the related strain $\varepsilon_{\max}$ were found by a cubic spline interpolation of computed σ_{uni} values. If no other instability precedes, the $\sigma_{\max}$ value can be considered to be the theoretical tensile strength σ_{iut} under corresponding superimposed biaxial stress.
4. The relaxation procedure was repeated for several preset σ_{bi} values.

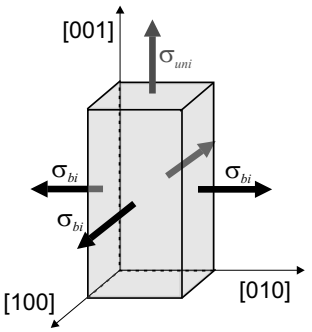

Figure 1.9 Illustration of a triaxial stress state that comprises a tensile stress in [001] direction σ_{uni} and superimposed transverse biaxial stresses σ_{bi}

The tensile strength of a majority of crystals increases almost linearly with the applied biaxial stresses (see Figure 1.10). The linear dependencies can be parametrized as

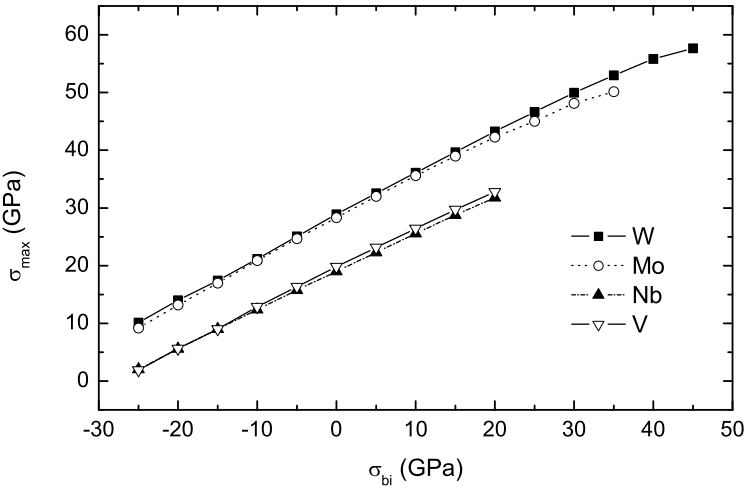

Figure 1.10 Dependence of the theoretical tensile strength $\sigma_{\max}$ on perpendicularly acting biaxial stresses σ_{bi} for W, Mo, Nb and V

$$\sigma_{\max} = \sigma_{\max,0} + k_{\max}\sigma_{bi}, \tag{1.19}$$

where $k_{\max}$ is the slope expressing the influence of the superimposed biaxial stress σ_{bi}. The parameters $k_{\max}$ are collected in Table 1.4. Values of the slope $k_{\max}$ seem to be higher for bcc crystals than for fcc ones.

Table 1.4 Slope of the linear regression lines $k = \dfrac{\mathrm{d}\sigma_{\max}}{\mathrm{d}\sigma_{bi}}$, maximum stress $\sigma_{\max,0}$ (GPa) and the ultimate strain $\epsilon_{\max,0}$ under pure uniaxial loading along with available literature data on σ_{iut} and computed values of theoretical isotropic strength σ_{iht} (GPa)

	$\sigma_{\max,0}$	$k_{\max}$	$\varepsilon_{\max,0}$	σ_{iut}	σ_{iht}
C	225	−1.08	0.37	225	88.5
Si	26.3		0.26		15.5
Ge	16.8		0.23		11.1
V	19.8	0.688	0.22		32.7
Fe	12.4	0.634	0.16	14.2	27.7
Ni	35.2		0.37	39.0	28.9
Cu	24.1		0.36	23.7	19.8
Nb	19.0	0.662	0.11	18.8	31.6
Mo	28.3	0.737	0.12	28.8	42.9
W	28.9	0.739	0.16	28.9	50.7
Ir	44.5	0.281	0.25		40.1
Pt	34.1	0.152	0.34		39.6
Au	18.6	0.163	0.33	22.5	23.2

A highly interesting exception of the studied elements is carbon with a diamond structure in which tensile strength decreases with increasing σ_{bi}. Thus, it exhibits a negative value of the slope $k_{\max} = -1.08$. An anomalous behaviour was also revealed in crystals of Si and Ge with a diamond structure and, to a certain extent, also in crystals of Ni and Cu. Both tensile and compressive applied biaxial stresses substantially reduce the σ_{iut}-values of Si and Ge (and less so those of Ni and Cu). Consequently, the $\sigma_{\max}$ *vs* σ_{bi} curves for Si and Ge exhibit sharp maxima near the zero applied σ_{bi} (see Figure 1.11) whereas the maximum of the diamond crystal is shifted by about 120 GPa towards the compressive region. This shift is a reason for the negative value of the slope $k_{\max}$ of the diamond crystal in the region around the zero value of σ_{bi}.

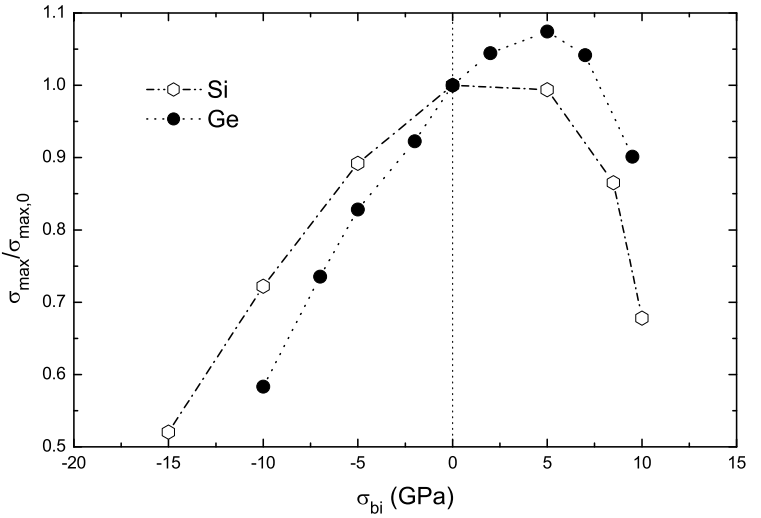

Figure 1.11 Normalized values of the theoretical tensile strength $\sigma_{\max}/\sigma_{\max,0}$ as functions of superimposed biaxial stress σ_{bi} for Si and Ge

One of practical consequences of the above-mentioned results is that the reinforcing fibres, subjected to tensile transverse stresses induced by incompatibility strains, can exhibit higher strength than those tested under uniaxial tension. In this way, a synergy effect can appear in composites (see Section 1.1.5).

Results concerning the dependence of the ultimate strain ε_u at the inflection point on the applied biaxial transverse stress were also obtained in the frame of the *ab initio* study. This dependence is depicted in Figure 1.12 for selected crystals. In general, the ultimate strain of fcc metals decreases with increasing biaxial stress (see the curves for Cu, Ni and Pt) whereas the opposite trend refers to bcc metals (Fe, Mo and V). The curves for dia-

mond structures C, Ge and Si exhibit maxima near the zero biaxial stress. The average ductility of fcc metals is higher than that of bcc crystals but, rather surprisingly, it is comparable to that of diamond crystals. This result shows that the behaviour of perfect crystals in terms of the ultimate strain is qualitatively different from that of engineering materials. In the latter case, indeed, the increasing biaxial stress always leads to a decrease of the ductility. This effect can be attributed to a plasticity driven growth and coalescence of microvoids that initiate at secondary phase particles (see Section 2.3). Thus, the lattice imperfections play a decisive role in the ductility response of engineering materials.

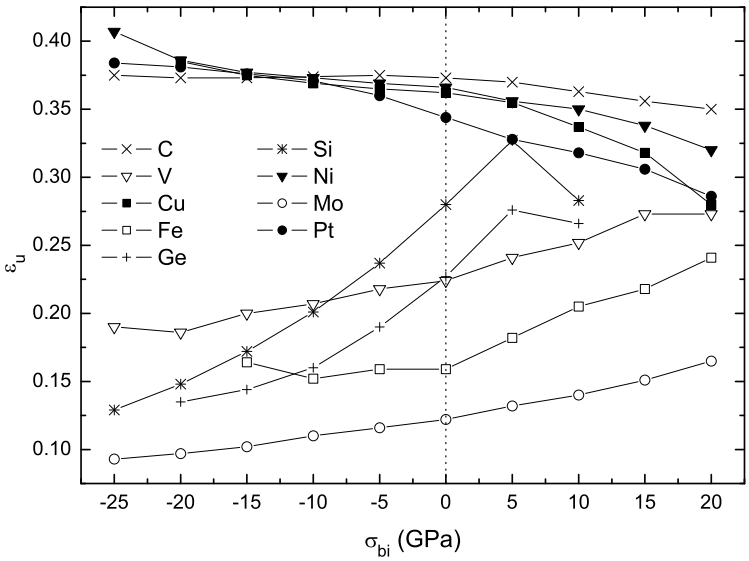

Figure 1.12 The ultimate uniaxial strain as a function of the applied transverse biaxial stress for selected perfect crystals

1.1.4.2 Coupling of Normal and Shear Stresses

Another important example of stress coupling is the influence of the stress component acting perpendicularly to slip planes during simple shear, as displayed in Figure 1.13 for a particular case of $\langle \bar{2}11 \rangle \{111\}$ shear in fcc lattice. Results of such analyses are presented in [59, 103, 106, 115, 116] for selected metallic, intermetallic and ceramic crystals. It should be noted that the relaxation procedure used in [116] comprised just a relaxation of atomic positions in the direction perpendicular to the slip planes but did not include the relax-

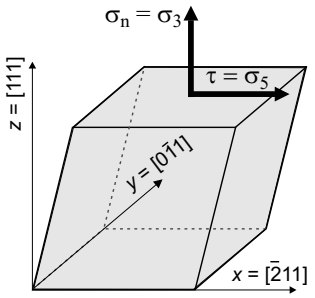

Figure 1.13 A crystal under superposition of shear and normal stresses

ation of ionic positions within the planes (in-plane relaxation). On the other hand, the in-plane relaxation was added to procedures used in [59, 103, 115].

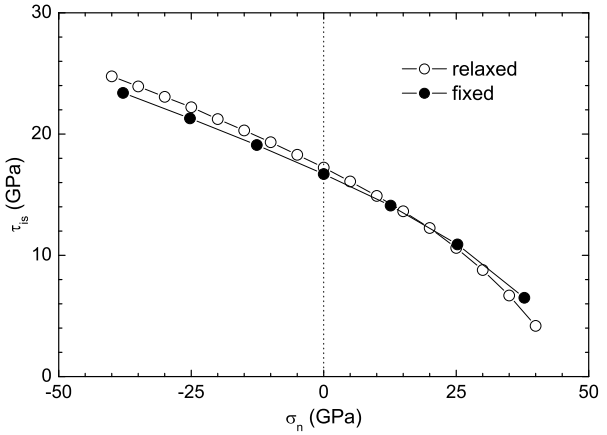

Figure 1.14 Influence of normal stress σ_n on the shear strength τ_{is} in Ir with and without in-plane relaxation

An example of results obtained for the crystal of iridium is shown in Figure 1.14. In general, the compressive normal force can substantially increase the shear strength. In the region of compressive normal stresses, the coupling effect can also be expressed by the linear function

$$\tau_{is} = \tau_{is,0} - b\sigma_n \tag{1.20}$$

in a formal analogy to the well known relation between the friction and the normal force exerted on sliding surfaces. In the region of tensile stresses, the coupling effect, at least for some crystals, changes to a parabolic shape (see Figure 1.14). This is in agreement with studies performed by Kelly *et al.* by means of empirical potentials [23].

In a more recent paper [118] six fcc crystals were subjected to homogeneous shear deformations in the {111} slip system in two distinct ways. In the first approach (from now on called the rigid-planes approach), the shear planes were kept undistorted during the whole shear process. Only the interplanar distance was allowed to change in order to set the normal stress to a prescribed value. This approach was consistent with previous calculations [23, 116]. However, the computed Hellman–Feynman stress tensor was used here instead of total energy calculations. The other approach (relaxed-planes) utilized a full relaxation of the stress tensor (including possible in-plane stresses). The details of the related computational procedure can be found in [59]. In both approaches, the main attention was paid to the tensile region of normal stresses. The homogeneous shear was simulated using a one-atom simulation cell.

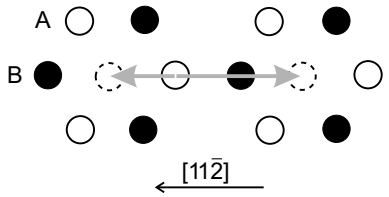

Figure 1.15 Two adjacent {111} A (*open circles*) and B (*solid circles*) planes in fcc crystals for illustration of the ⟨112⟩{111} shear system

The shear system studied is illustrated in Figure 1.15. For the sake of clarity, only two adjacent planes are displayed. When the upper plane A moves to the right, its atoms must overcome a high-energy barrier related to over-passing the atoms in the B plane. The final position of the selected atom in plane A is marked by the dashed circle. The corresponding structure has fcc symmetry of an opposite stacking order (with respect to the original state). The same state can be reached by moving the A plane to the left. In this case, the corresponding energy barriers as well as the related stresses are substantially lower. Although the plane shift cannot then continue the same path (because of the consequent higher energy barrier), the instant of approaching the shear strength is the first onset of instability. For the calculations of Hellman–Feynman stress tensor the Vienna *Ab initio* Simulation Package (VASP) was utilized. In the case of Ni, the projector augmented-wave potential was used along with the spin-polarized calculations taking the ferromagnetic ordering into account. The exchange-correlation energy was evaluated using either the local density approximation (Pt, Au) or the generalized-gradient approximation (Al, Ni, Cu, Ir). The functions $\tau_{is}(\sigma_n)$ were found to be almost linearly decreasing and could also be expressed by Equation 1.20. The regression parameters are collected in Table 1.5. When comparing the computed data with the previously published results [116] one can see good agreement in $\tau_{is,0}$ values while more significant differences can

be found in b values. They are probably caused not only by a different assessment but also by a differently selected range of interpolated data with respect to normal stresses. Nevertheless, all the b values match the previous results within 15%.

Table 1.5 Regression parameters for {111} shear strength in both the rigid-planes and the relaxed-planes approaches

Element	Rigid-planes		Relaxed-planes		
	$\tau_{is,0}$ (GPa)	b	$\tau_{is,0}$ (GPa)	b	$\tau_{is,0}$ [a] (GPa)
Al	3.12	0.238	3.07	0.319	2.84
Ni	5.64	0.139	5.05	0.123	5.05
Cu	3.01	0.117	2.43	0.080	2.16
Ir	17.1	0.223	17.3	0.249	
Pt	2.75	0.138	2.05	0.177	
Au	1.66	0.152	1.05	0.171	0.85

[a] [99]

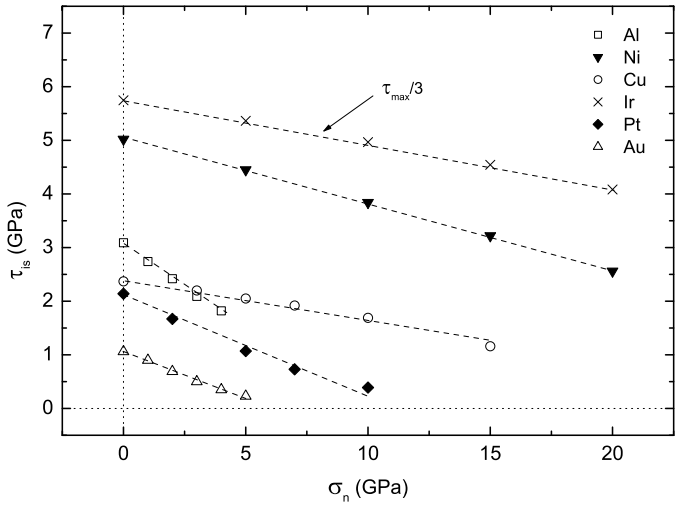

Figure 1.16 Theoretical shear strength as a function of normal stress in the relaxed-planes approach. *Dashed lines* represent linear regressions of the displayed data points

The results of relaxed-planes calculations are displayed in Figure 1.16. Again, the $\tau_{is}(\sigma_n)$ curves can be approximated by linear functions up to $\sigma_n = 20\,\text{GPa}$. The regression parameters are also included in Table 1.5. By comparing both approaches one can see that the full relaxation of stresses lowers the shear strength of all investigated crystals except for iridium.

Crystals of metals and diamond exhibit a nearly linear decrease in the ideal shear strength with increasing superimposed isotropic (hydrostatic) stress σ_h [55,119]. This behaviour seems to be closely related to the fact that, during a pure shear ($\sigma_h = 0$), the lattice volume of these crystals increases, thus minimizing the crystal energy. An application of the tensile isotropic stress works, therefore, as a shear driving force leading to a reduction of the ideal shear strength. On the other hand, the lattice volume of covalent crystals Si, Ge and SiC decreases during the pure shear so that the dependence $\tau_{is}(\sigma_h)$ exhibits an opposite trend [106]. This reasoning can be, to a large extent, also applied to the $\tau_{is}(\sigma_n)$ dependence. However, the ideal shear strength of Cu and Ni crystals is lowered by both tensile and compressive normal stresses [55,119]. This anomalous behaviour can be understood from the crystal relaxation during the shearing process. Under the pure shear deformation, these crystals prefer to extend the shear planes perpendicularly to the shear direction rather than increase their interplanar distance. Consequently, an application of additional compressive normal stresses contributes to further lateral extension that makes the shear easier [55, 59, 120].

1.1.4.3 Calculation of Tensile Strength from Shear Strength Data

The application of mechanical-stability criteria to the prediction of ideal tensile strength is computationally very time-consuming. These criteria can be interpreted approximately by assuming that a rupture of perfect crystals under uniaxial tension starts when reaching the shear strength in some convenient shear system [102]. An illustration of such a shear system in a crystal sample is given in Figure 1.17.

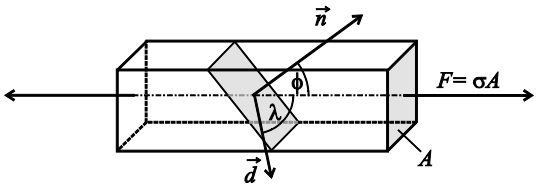

Figure 1.17 Illustration of a shear system in a crystal sample under tensile stress. The angles ϕ and λ are measured between the crystal axis and the normal **n** of the slip plane and the slip direction **d**, respectively. Reprinted with permission from Institute of Physics and IOP Publishing Ltd. (see page 265)

When the crystal is subjected to tensile stress, certain slip systems can be exposed to a combination of shear and tensile (normal to the shear plane) stresses. The displayed vectors **n** and **d** determine the vertical to the shear plane and the shear direction, respectively. The normal stress σ_n can be

expressed by means of the tensile stress σ and the angle ϕ as

$$\sigma_n = \sigma \cos \phi. \tag{1.21}$$

Assuming that some shear instability can precede the volumetric instability, the ideal tensile strength σ_{iut} can be estimated from the corresponding theoretical shear strength τ_{is} using the relationship

$$\sigma_{iut,s} = \frac{\tau_{is}}{\cos \phi \cos \lambda}. \tag{1.22}$$

The relation is similar to the well known Schmid's law

$$\tau_c = \sigma_y \cos \phi \cos \lambda \tag{1.23}$$

that expresses the relationship between the critical resolved shear stress τ_c required to move dislocations across the slip plane and the yield stress σ_y in a crystal with dislocations. However, Equation 1.22 holds only for a perfect single crystal. Another significant difference between Equations 1.22 and 1.23 lies in the influence of the normal stress on the critical shear stress. Whilst, in Schmid's law, the critical shear stress does not depend on the normal stress σ_n (at least in fcc crystals), the significant influence of σ_n on the ideal shear strength has already been clearly demonstrated. The latter result can be used for a simple estimate of σ_{iut} for fcc crystals Al, Ni, Cu, Ir, Pt and Au.

In order to estimate the theoretical tensile strength σ_{iut}, Equations 1.20, 1.21 and 1.22 can be combined into the final form

$$\sigma_{iut,s} = \frac{\tau_{is,0}}{\cos \phi(\cos \lambda + b \cos \phi)} \tag{1.24}$$

when assuming $\sigma = \sigma_{iut,s}$ in Equation 1.21. Equation 1.24 can easily be used for an estimation of the ideal tensile strength from the ideal shear strength $\tau_{is,0}$.

The $\sigma_{iut,s}$ values obtained for uniaxial tension in [110], [11$\bar{1}$] and [100] directions are listed in Tables 1.6 and 1.7. Uniaxial tension was applied to the crystal in the most favourable representative of the family of symmetry-equivalent directions $\langle 110 \rangle$, $\langle 111 \rangle$ and $\langle 100 \rangle$. The σ_{iut} values, that were collected from available literature, represent the corresponding values of the volumetric-instability stress (at the inflection point). It can be seen that the predicted $\sigma_{iut,s}$ values for [100] and [11$\bar{1}$] directions are substantially lower than the corresponding σ_{iut} values for all studied fcc crystals with the exception of Ir. On the other hand, the σ_{iut} values in [110] direction are so low that the predicted $\sigma_{iut,s}$ values are of a comparable magnitude. In the case of [100] direction, the predicted $\sigma_{iut,s}$ values for Cu, Ni and Al can be well compared with ideal strength σ^*_{iut} corresponding to the first onset of the mechanical instability as predicted in [78,98] or the phonon instability as reported in [101].

Table 1.6 The estimated theoretical tensile strengths $\sigma_{iut,s}$ in $\langle 110 \rangle$ and $\langle 111 \rangle$ directions (in GPa) along with the available literature data for σ_{iut} (volumetric instability)

Element	$\langle 110 \rangle$ loading			$\langle 111 \rangle$ loading		
	$\sigma_{iut,s}^{\text{rigid}}$	$\sigma_{iut,s}^{\text{relaxed}}$	σ_{iut}	$\sigma_{iut,s}^{\text{rigid}}$	$\sigma_{iut,s}^{\text{relaxed}}$	σ_{iut}
	[GPa]	[GPa]	[GPa]	[GPa]	[GPa]	[GPa]
Al	5.0	4.5	4.2[a]	9.2	8.8	14.8[a]
Ni	10.0	9.1	11.7[a]	17.1	15.4	39.3[a]
Cu	5.5	4.6	5.5[a]	9.2	7.5	26.5[a]
Ir	27.6	27.1	26.5[b]	50.4	50.6	43.5[b]
Pt	4.9	3.5		8.3	6.1	30.0[b]
Au	2.9	1.8	2.8[a]	5.0	3.2	13.6[a]

[a] [78]
[b] [102]

Table 1.7 The estimated theoretical tensile strengths $\sigma_{iut,s}$ in $\langle 100 \rangle$ direction along with the available literature data for the ideal strength σ_{iut} (volumetric-instability) and the ideal strength σ_{iut}^{*} corresponding to the first onset of the shear instability

Element	$\sigma_{iut,s}^{\text{rigid}}$	$\sigma_{iut,s}^{\text{relaxed}}$	σ_{iut}^{*}	σ_{iut}	
	[GPa]	[GPa]	[GPa]	[GPa]	
Al	9.9	9.0	11.1[a]	12.6[a]	
Ni	20.0	18.3	21.3[a]	39.0[a]	35.2[b]
Cu	11.0	9.3	9.8[a]	23.7[a]	24.1[b]
Ir	55.2	54.3		44.5[b]	
Pt	9.8	7.0		34.1[b]	
Au	5.8	3.6	10.0[a]	22.5[a]	18.6[b]

[a] [78]
[b] [98]

A good agreement of results predicted from shear strength data with those obtained by including the stability analysis also seems to be promising for an application of the proposed method to crystals other than fcc.

1.1.5 Nanocomposites

Composites represent a widely used successful way to improve mechanical characteristics of materials, in particular their elastic moduli, strength and fracture toughness. Resulting properties in real engineering macro-composites are functions of many parameters depending on the particular design and production technology. However, the situation is not so complicated for all

mechanical characteristics. For example, the Young's modulus of long-fibre composites in the direction of the fibre can be sufficiently precisely assessed according to the following simple relationship:

$$E = \eta V_f E_f + (1 - V_f) E_m, \tag{1.25}$$

where E_f and E_m are Young's moduli of the fibre and the matrix, respectively, V_f is the volume fraction of fibres and η is the factor depending on the strength of cohesion of the fibre/matrix interface [121]. Obviously $\eta = 0$ when there is no cohesion at all, while $\eta = 1$ corresponds to the ideal binding between atoms of matrix and fibres. The value $\eta \approx 0.8$ is fulfilled for a majority of real composites of a standard quality. Similar simple linear relationships are also often used for other moduli as well as for the strength of composites.

Values of the equilibrium volume, elastic moduli and σ_{iut} of ideal nanocomposites were computed in [122–124] for different thicknesses of nanofibres from a single atom to several atomic distances. The fibres were made of W or Mo, whereas the matrix consisted of V or Nb atoms. In these first principles studies, the uniaxial tensile loading was applied parallel to the nanofibres. The main aim was to verify the validity of Equation 1.25 for elastic moduli and σ_{iut} in the ideal case of $\eta = 1$.

1.1.5.1 Calculation Method

A model of the nanocomposite was built up as a periodic repeating of $4 \times 4 \times 1$ bcc-based super-cell which is displayed in Figure 1.18 for the Nb–W composite. The crystal super-cell contained 32 atoms in both A (solid circles) and B (open circles) (001) planes. The grey solid circles in Figure 1.18 belong to other (adjacent) super-cells. The dashed contours define interfaces between the wires (W) and the matrix (Nb) in investigated lamina models of different concentrations (percentages) of wire atoms. In order to get a few more different concentrations, the systems Nb (wires) and W (matrices) were also studied. In this way, additional wire concentrations of 59.4%, 71.9% and 84.4% could be obtained.

The calculation procedure consisted of several steps. The first step was a computation of the total energy E_{tot} per atom as a function of the atomic volume V. Atomic positions within the cell had to be relaxed in order to minimize the interfacial stresses. The equilibrium volume per atom V_0 of each lamina model was obtained from the energy minimum and the lamina bulk modulus B could be determined according to Equation 1.18 ($U = E_{tot}$). Then the crystal system was elongated in the [001] direction to simulate uniaxial loading applied in the direction parallel to the lamina fibres. The system energy was minimized at any elongation by a full relaxation procedure regarding the atomic positions within the super-cell. The dependence of the total energy obtained on the relative elongation ε allowed authors to compute

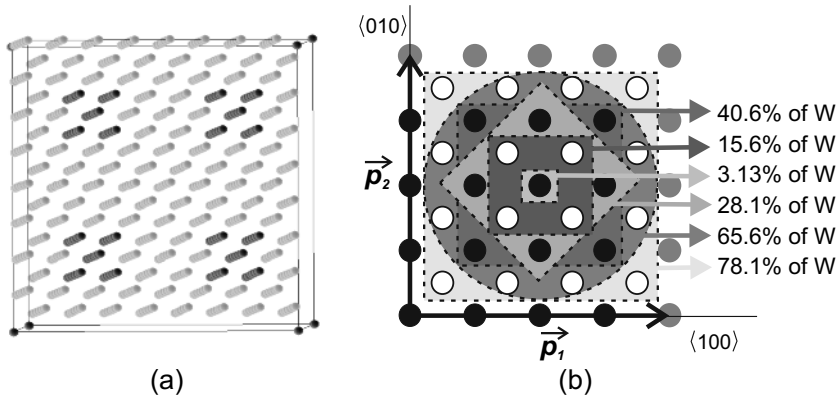

Figure 1.18 A sample of: (a) the nanocomposite, and (b) the super-cell

the values of the uniaxial stress σ applied to the system as well as the Young's modulus E_{001} value:

$$\sigma = \frac{1}{V}\frac{\mathrm{d}E_{tot}}{\mathrm{d}\varepsilon}$$

and

$$E_{001} = \frac{1}{V_0}\frac{\mathrm{d}^2E_{tot}}{\mathrm{d}\varepsilon^2}. \tag{1.26}$$

If no other instability precedes, the uniaxial stress reaches its maximum at the point of inflection of the E_{tot} function and the related stress σ_{iut} can be considered to be the IS of the nanocomposite under the conditions of uniaxial loading.

For electronic structure calculations the VASP code was utilized. The cut-off energy for the basis set was 290 eV and the exchange-correlation energy was evaluated using the generalized-gradient approximation of Perdew and Wang with Vosko, Wilk and Nusair interpolation [125]. The $3 \times 3 \times 12$ k-points mesh was used in all calculations. The solution was considered to be self-consistent when the energy difference of two consecutive iterations was smaller than 0.1 meV. Atomic positions within the super-cell were relaxed using the Hellman–Feynman stress tensor.

1.1.5.2 Computed Data for Composite Constituents

Although it could have been possible to compute the data for pure tungsten, vanadium and niobium using a primitive cell, the super-cell with all atomic positions occupied by the same kind of atoms was used in the calculations. This allowed us to check the results for the composites in a more reliable way.

Computed values of the equilibrium lattice parameter a_0, the bulk modulus B, the shear modulus G, the Young's modulus E_{001} and the Poisson's ratio ν for pure W, Nb, Mo and V are listed in Table 1.8 along with experimental data. The experimental values of a_0 and B were taken from [126]. Values of E_{001} and ν were computed from experimentally determined elastic moduli [82,127] using Equations 1.8 and

$$\nu = \frac{C_{12}}{C_{11} + C_{12}}.$$

Table 1.8 Ground-state properties of Nb, W, Mo and V along with their ideal uniaxial strengths

Element		a_0 [Å]	B [GPa]	E_{001} [GPa]	ν	σ_{iut} [GPa]	
Nb	calc.	3.32	177	127	0.38	19.2[a]	18.8[b]
	exp.	3.30	170	152	0.35		
W	calc.	3.18	318	389	0.29	28.8[a]	28.9[c]
	exp.	3.16	323	417	0.28		
V	calc.	2.98	188	199	0.32	19.9[a]	
	exp.	3.03	162	151	0.34		
Mo	calc.	3.15	268	412	0.24	28.3[a]	28.8[b]
	exp.	3.15	272	394	0.26		

[a] [122]
[b] [49]
[c] [41]

The agreement between computed and experimental values of a_0 is excellent (within 1%). In spite of a most noticeable exception of the Young's modulus for Nb (underestimated by 16%), the agreement is very good also in the case of elastic moduli and the Poisson's ratio (mostly within 5%).

Computed values of the uniaxial stress σ_{iut} at the point of inflection on the $E_{tot}(V)$ curve for pure Nb, W, V and Mo are listed in Table 1.8 along with available literature data. The mutual agreement of values from different sources is very good.

1.1.5.3 Solutions for Composites

As an example, the dependence of the average atomic volume V_0 on the atomic concentration of W (nearly corresponding to the volume fraction V_f of tungsten fibres) in the niobium matrix is depicted in Figure 1.19 by solid squares. The dotted line interpolates between experimental values for pure Nb and W. As can be expected, the atomic volume linearly decreases with W concentration. Similar dependencies also hold for other studied composites.

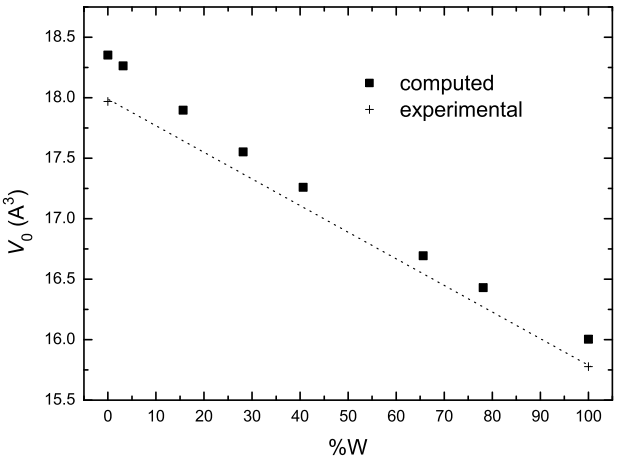

Figure 1.19 Equilibrium atomic volume as a function of W concentration

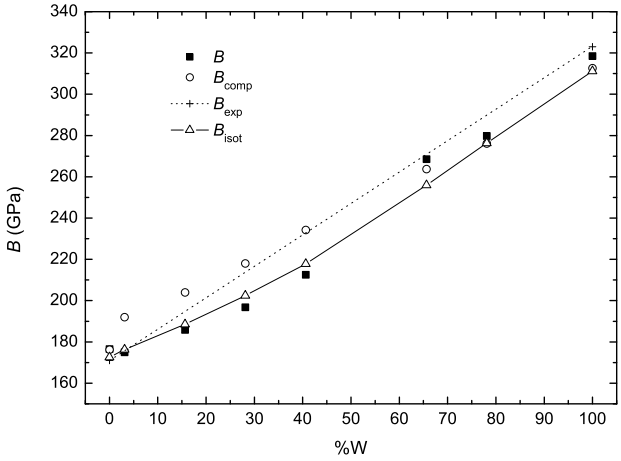

Figure 1.20 The composite bulk modulus as a function of the atomic concentration of tungsten fibres

The dependence of the composite bulk modulus B on the atomic concentration of W is depicted in Figure 1.20. Values obtained by means of Equation 1.26 are displayed by open circles. The triangles show values of B calculated from the Equation 1.27 (valid for an isotropic material)

$$B_{\text{isot}} = \frac{E_{001}}{3(1-2\nu)} \tag{1.27}$$

by using E_{001} values computed according to Equation 1.26. Both of them seem to follow Equation 1.25, where the bulk moduli are used instead of

E_{001}. The dotted line in Figure 1.20 follows Equation 1.25 for experimental values $B_f = 323\,\text{GPa}$ and $B_m = 170\,\text{GPa}$.

Values of the Young's modulus E_{001} of all investigated composites were also found to follow the linear mixture rule in a satisfactory manner. Consequently, all atomistic results confirm that deviations from Equation 1.25 observed for real composites are caused by their imperfections, in particular by a reduced interface cohesion.

While the computed quantities such as the equilibrium volume or elastic moduli obey the simple linear mixture rule, the IS of a pure reinforcing materials W and Mo can already be reached (or even exceeded) well below the 100% concentration of the fibres in the composite. Indeed, Figure 1.21 displays the σ_{ip} values as functions of the reinforcement concentration for all the investigated composites. The curves exhibit a simple linear dependence on the atomic concentration of fibre atoms up to about 60–80%. Above this concentration range they seem to reach a saturated value.

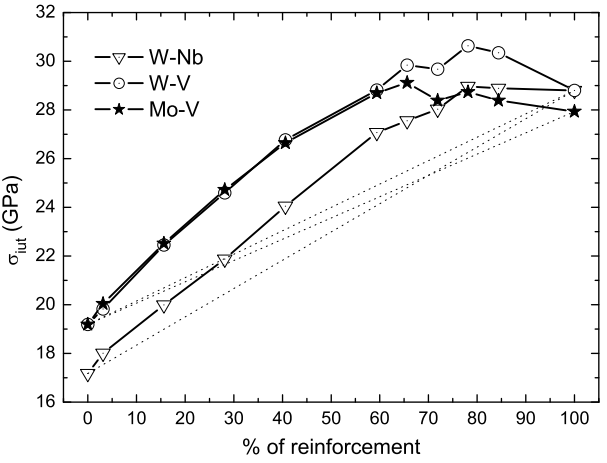

Figure 1.21 Theoretical tensile strength as a function of atomic concentration of reinforcing fibres for three composites. The fibres are made of W or Mo, whereas the matrix consists of V or Nb atoms

A possible explanation of this synergy effect can be the lattice mismatch owing to different Poisson's contractions of individual composite constituents. As a consequence, the fibres can be under transverse tensile or compressive stresses which can influence the uniaxial tensile strength of the whole composite (see Section 1.1.4). It was found that, in the case of cubic metals, the tensile strength increases under conditions of superimposed tensile transverse stresses. Therefore, a simple model has been developed to verify the above-mentioned explanation of the synergy effect in nanocomposites [128]. The model compares the data obtained for V–W nanocomposites with those achieved by modelling a deformation behaviour of two independent ideal

crystals of pure W and V. In order to include the stress coupling effect, the individual crystals were loaded in a triaxial mode that simulated the stress state experienced by the fibre or the matrix in the composite. It was found that, during the deformation, the vanadium matrix was subjected to transverse (internal) tensile biaxial stress whereas the tungsten fibres experienced compressive stresses. By including these stresses into the simple proportional rule written in terms of stresses acting on the nanocomposite, the σ_{iut} values shift above the linear function interpolating strengths of W and V (the corresponding dotted line in Figure 1.21). However, such a shift does not fully reproduce the computed σ_{iut} values of the composite which means that either the predicted synergy effect is not only caused by the internal transverse stresses or the applied model is not sufficiently precise. Let us finally mention that the procedure simulating the deformation of the nanocomposite can also be improved by including a relaxation of all atomic positions within the bulk. These issues should be a matter of further analyses.

1.1.6 Influence of Crystal Defects and Temperature

All preceding results concerning the IS were obtained assuming a perfect crystal and an extremely low temperature ($T \to 0$). In real perfect crystals (whiskers), however, the presence of some imperfections is to be expected. At least, an equilibrium concentration of vacancies as well as a certain level of surface roughness are inevitable. Thus, it is worthwhile to assess possible effects of lattice defects, surface roughness and temperature on IS. For principal reasons, however, the strength of imperfect crystals cannot be identified as IS any more. Therefore, the term "strength" will simply be used instead of IS hereafter.

In general, the presence of lattice defects decreases the strength value. The only exception to this rule might be some special impurity dopants and alloying atoms. Since no grain (or subgrain) boundaries and secondary phase particles are expected in perfect single crystals, only point defects, dislocations, stacking faults, twins, free surfaces, cracks and phonons (temperature) are mentioned in the following brief summary.

1.1.6.1 Crystal Defects

Vacancies are inevitable in real crystals just near the zero Kelvin temperature. However, the effect of monovacancies on strength is negligible which simply follows from Equations 1.2 for σ_{iut}. Indeed, this classical formula for the tensile IS is equal to the Griffith criterion for a nanocrack of an atomic size – a vacancy. Larger clusters of vacancies (microcracks) may probably exist only

at temperatures near the melting point that are far beyond the temperature range relevant for strength studies.

The effect of impurities and alloying atoms was studied in several works based on *ab initio* methods. Although Goodwin *et al.* [129] found that Ge and As impurities in aluminium raise the cohesive energy by up to 8%, no clear conclusions concerning the change in strength were made. Huang *et al.* [130] reported no effect on the σ_{iut} value of silicon in the case of p-type doping, unlike the 6% decrease in the case of very high levels of n-dopants. Both works used the pseudopotential approach combined with molecular dynamics. Song *et al.* [100] used the DVM method to realize that the 7% alloying of V, Cr, Fe and Mo slightly improves the value of σ_{iht}, unlike the 4% alloying that caused a slight decrease in σ_{iht}. Many authors (e.g., [131]) theoretically expect a slight decrease in τ_{is} owing to the impurity content. In summary, the influence of a low concentration of point defects on the strength seems to be very small.

Dislocation slip appears when shear stress in the slip plane parallel to the slip direction reaches the Peierls–Nabarro level. Since this level in metals is relatively very low, the strength might be dramatically reduced (by four orders of magnitude or even more). On the other hand, the P-N stress is extremely high in ceramic covalent crystals (C, Si, SiC, ZnS, Si_3N_4) as well as in complex ionic crystals ($MgAl_2O_4$, Al_2O_3, Al_2O_3.MgO). The dislocations are practically sessile at near zero temperatures and, therefore, the tensile strength might be reduced only by tens of percents owing to microcracks initiated by the stress relaxation around dislocations with long Burgers vectors.

As far as we know, no special studies regarding the effect of stacking faults (SF) on strength have been performed. Atoms on the stable SF plane lie in the local energy minimum and no stress is induced in the surrounding volume. The energy of the SF per atom is about two orders of magnitude lower than that of the free surface. We may, therefore, deduce that the influence of SFs on strength can be neglected. This also refers, most probably, to twins as was shown for the NiTi crystal from first principles [132].

The effect of a perfectly flat free surface on the strength can also be considered to be negligible. However, small imperfections like scratches or dimples act as stress concentrators (micronotches). Their maximum effect on strength can be roughly estimated by a factor $1+2(l/\rho)^{1/2}$, where l is the notch depth and ρ is the curvature of the notch root ($\rho > 0$) [133]. Therefore, sharp notches can significantly reduce the strength value.

According to the Griffith law for perfectly brittle materials, an atomically sharp crack of length a causes a drop in the tensile strength value by a factor of $(2a_0/(\pi a))^{1/2}$ (a_0 is the lattice parameter). However, only ceramics, semiconductors and, most probably, molybdenum and tungsten can be considered to be intrinsically brittle crystals at absolute zero temperature (see Section 1.2). In all other metals, dislocation emission precedes unstable crack growth. This process increases the effective surface energy and blunts the crack tip

(see Chapter 2). Consequently, the strength drop must be much less than that predicted by the Griffith law.

1.1.6.2 Temperature

The variation of strength with temperature is generally attributed to the role of phonons in deformation and fracture processes. Although the Frenkel formula at Equation 1.1 simply suggests that the variation should be the same as that of the shear modulus, the Orowan–Polanyi relation at Equation 1.2 brings a complication with the temperature dependence of the surface energy. From a historical point of view, two sufficiently relevant methods were applied to predict the temperature influence: the Einstein model of harmonic oscillators combined with the elastic instability criterion and the model of dislocation nucleation supported by phonon fluctuations [1]. The first approach predicted a drop in the uniaxial strength within the range of units to tens of percents when changing the temperature from 0 K to 1000 K. The results depend on the type of utilized interatomic potentials (short- or long-range). However, this drop was found to be very close to that predicted when considering only the change in Young's modulus. The second approach deals with the maximum energy of up to $50\,kT$ (k is the Boltzmann constant) that the thermal fluctuations can supply at any temperature. Typically, the results reveal tens of percents decrease in the strength within that temperature range. An analysis of a possible thermal crack initiation has shown that relatively small amounts of available thermal energy are unlikely to affect the process very much up to 1200 K (in comparison with the total amount of strain energy conversion into surface energy). It should be emphasized, however, that the most physically justified approaches to the temperature problem are complex analyses of phonon spectra or the quantum (*ab initio*) MD simulations. However, recently available studies of that kind are too rare and incomplete to allow general conclusions.

Nevertheless, one can assume that the temperature change in the relevant elastic modulus might be considered to be an acceptable lower-band approximation to the strength-temperature dependence.

1.2 Intrinsic Brittleness and Ductility

The intrinsic tendency of perfect crystals to brittleness or ductility can be quantitatively assessed by considering crack stability conditions. Indeed, when a cracked crystal is subjected to a tensile loading, there are basically two possibilities for its behaviour – either an unstable cleavage fracture is observed (brittleness) or a dislocation emission stabilizes the crack tip by plastic blunting (ductility). Physical solutions of that problem are usually constructed by

means of two classical approaches introduced by Kelly *et al.* [23] and Rice and Thompson [134]. The former deals with the ratio of tensile to shear ideal strengths σ_{iut}/τ_{is} of an investigated crystal, whereas the latter analyses a related mechanism of dislocation emission. The principles of both concepts, which lead to essentially equivalent results, are outlined in the following subsection along with a description of more general approaches. Further parts are devoted to an extended calibration of crystal brittleness/ductility performed by Rice *et al.* [135] and, in particular, to that developed by us.

1.2.1 Fundamentals

1.2.1.1 Classical Criteria

The classical understanding of intrinsic brittle/ductile behaviour was introduced by Kelly, Tyson and Cottrell (KTC) [23]. According to this concept, the crystal is considered to be intrinsically ductile when τ_{is} is exceeded earlier than the σ_{iut} at the crack tip. This corresponds to the following condition of intrinsic ductility:

$$\frac{\sigma_1 \tau_{is}}{\sigma_{iut} \tau_r} < 1, \tag{1.28}$$

where σ_1 is the maximum principal stress and τ_r is the resolved shear stress on the active slip plane adjacent to the crack tip. However, only slip in crystallographic planes containing the whole crack front can effectively produce blunting. Let us consider the blunting configuration depicted in Figure 1.22 in a special case of mode I loading (the shear stress intensity factors $K_{II} = K_{III} = 0$). Then, Equation 1.28 can be rewritten as

$$\frac{\sigma_{iut}}{\tau_{is}} > \frac{2[1 + \sin(\Theta/2)]}{\sin\Theta \cos\Phi}, \tag{1.29}$$

where Θ is the angle between the crack plane and the intersecting slip plane and Φ is the angle between the Burgers vector and the direction perpendicular to the crack front [136].

The following reasoning leads to a derivation of Equation 1.29. The stress tensor at the crack tip under the condition of plane strain [137] reads

$$\tau_{ij} = \begin{pmatrix} A\left[1 - \sin\left(\frac{\Theta}{2}\right)\sin\left(\frac{3\Theta}{2}\right)\right] & A\sin\left(\frac{\Theta}{2}\right)\cos\left(\frac{3\Theta}{2}\right) & 0 \\ A\sin\left(\frac{\Theta}{2}\right)\cos\left(\frac{3\Theta}{2}\right) & A\left[1 + \sin\left(\frac{\Theta}{2}\right)\sin\left(\frac{3\Theta}{2}\right)\right] & 0 \\ 0 & 0 & 2A\nu \end{pmatrix},$$

where

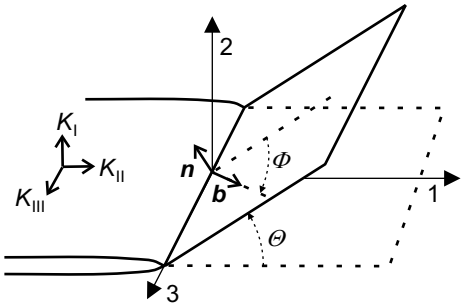

Figure 1.22 Scheme of the blunting crack-slip plane configuration

$$A = \frac{K_I}{\sqrt{2\pi r}} \cos\left(\frac{\Theta}{2}\right)$$

and

$$\sigma_1 = A\left[1 + \sin\left(\frac{\Theta}{2}\right)\right]. \tag{1.30}$$

Regarding Figure 1.22, the coordinates of the stress vector $\mathbf{T}$ in the slip plane can be expressed by means of the stress tensor τ_{ij} and the normal $\mathbf{n} = (-\sin\Theta, \cos\Theta, 0)$ as $T_i = \tau_{ij} n_j$ which gives

$$\mathbf{T} = (T_1, T_2, T_3) = \left(-\frac{A}{2}\sin\Theta, A\cos^2\left(\frac{\Theta}{2}\right), 0\right).$$

The magnitude of the resolved shear stress τ_r depends on τ_{ij} and $\mathbf{b} = (\cos\Theta\cos\Phi, \sin\Theta\cos\Phi, \sin\Phi)$ as

$$\tau_r = \mathbf{T} \cdot \mathbf{b} = \frac{A}{2}\sin\Theta\cos\Phi. \tag{1.31}$$

By substituting Equations 1.30 and 1.31 into the criterion at Equation 1.28 one finally obtains Equation 1.29.

Another criterion based on the ability of the material to emit dislocations from the crack front was proposed by Rice and Thomson (RT) [134]. There are two principal forces acting on the emitted dislocation in the adjacent slip plane. The first is the repulsive force that is induced by external loading and the second is the attractive mirror force induced by a presence of free surfaces (crack flanks). In the frame of the elastic approximation and in terms of the K_I factor, the resulting force component within the slip plane can be expressed as follows:

$$f_d(r) = \frac{b_e}{2\sqrt{2\pi r}} K_I \sin\Theta\cos\frac{\Theta}{2} - \frac{G}{4\pi r}\left(b_s^2 + \frac{b_e^2}{1-\nu}\right), \tag{1.32}$$

where b_e and b_s are magnitudes of edge and screw components of the Burgers vector, respectively, and G is the shear modulus. The function at Equation 1.32 is schematically plotted in Figure 1.23. One can see that for small distances of the dislocation from the crack front ($r < r_0$, where $f_d(r_0) = 0$) the attractive force is dominating, whereas for greater distances the repulsive interaction prevails. This means that the elastic theory always predicts a mechanical instability, i.e., the intrinsic brittleness. However, the elastic approximation fails for $r \leq r_c$, where r_c is the size of the dislocation core. In this case the Burgers vector of the emitted dislocation is expected to be proportional to r and, consequently, the repulsive force remains dominating over the whole distance. In other words, the condition $r_0 \leq r_c$ means a spontaneous emission of dislocations and, with regard to Equation 1.32 and $r_0 = r_c$, the stress intensity factor corresponding to this emission can be written as

$$K_{Ie} = \frac{G}{\sqrt{2\pi r_c}} \frac{b_s^2 + b_h^2/(1-\nu)}{b_h \sin\Theta \cos(\Theta/2)}.$$

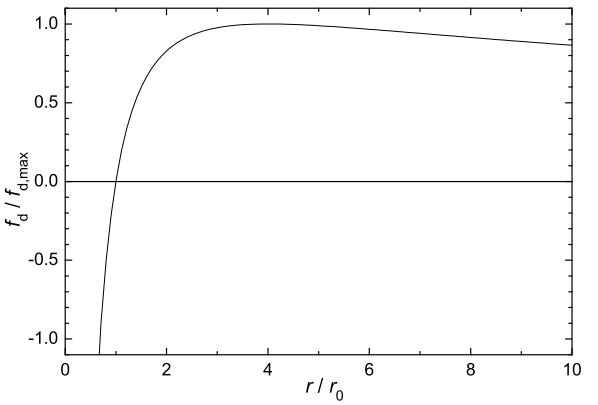

Figure 1.23 The dependence of the resulting force on the relative distance for a dislocation emitted from the crack front

Because the Griffith criterion for brittle fracture reads

$$K_{Ic} = \sqrt{\frac{2G\gamma}{1-\nu}},$$

where γ is the fracture energy, the combined criterion for intrinsic ductility becomes

$$K_{Ie} < K_{Ic}. \tag{1.33}$$

Note that no thermal activation was assumed to help the dislocation emission in the RT concept which corresponds to absolute zero temperature. This

means that Equation 1.33 overestimates the tendency of crystals to intrinsic brittleness when applied to higher temperatures.

At zero Kelvin, the criteria KTC and RT are essentially equivalent and yield similar results (see later). Indeed, when one assumes remote mode I loading, the simplest IS estimates at Equations 1.1 and 1.2 and an averaged angle $\bar{\Theta}$ [138], both criteria can be rearranged to

$$\frac{Gb}{10\gamma} < 1.$$

1.2.1.2 Beyond the Classical Criteria

The efficiency of both criteria in their classical forms is restricted in many directions. First, there is only one selected configuration of crack-slip planes. In the KTC criterion, moreover, the Orowan estimate of σ_{iut} contains an uncertain γ-value and it does not reflect the real triaxial state of stress at the crack tip. The Frenkel formula for τ_{is} does not take the normal/shear stress coupling into account. Second, the RT criterion contains a purely defined r_c-value and stands only for the mode I case. Therefore, more generalized and accurate approaches are needed in order to obtain a plausible calibration of crystals with respect to their intrinsic brittle/ductile response.

The RT-criterion was upgraded by application of the Peierls–Nabarro model to the process of the dislocation nucleation as well as by replacing the K_I-concept by that of the effective crack driving force G_{eff} [135, 139] (see also Appendix B). This leads to the following condition for dislocation nucleation:

$$\begin{aligned}\Big[f_I(\Theta)K_I + f_{II}K_{II}\Big]\cos\Phi + f_{III}(\Theta)K_{III}\sin\Phi = \\ = \sqrt{\frac{2G}{1-\nu}\left[\cos^2\Phi + (1-\nu)\sin^2\Phi\right]\gamma_b},\end{aligned} \tag{1.34}$$

where K_I, K_{II} and K_{III} are stress intensity factors (SIFs) for modes I, II and III, f_I, f_{II}, f_{III} are related angular functions and γ_b is the energy barrier for the dislocation nucleation. In the case of a pure opening mode I Equation 1.34 reduces to

$$G_I = 8\frac{1 + (1-\nu)\tan^2\Phi}{(1+\cos\Theta)\sin^2\Theta}\gamma_b,$$

where $G_I = (1-\nu)K_I^2/2G$.

The intrinsic ductility means that, during the loading, Equation 1.34 is satisfied earlier than the generalized Griffith condition $G_{eff} = 2\gamma$. This leads to

$$\frac{\gamma}{\gamma_b} > \frac{4[1 + x^2 + z^2/(1-\nu)][1 + (1-\nu)\tan^2 \Phi]}{(1 + \cos\Theta)[\sin\Theta + (3\cos\Theta - 1)x + 2z\tan\Phi]^2}, \tag{1.35}$$

where $x = K_{II}/K_I$ and $z = K_{III}/K_I$. In the case of the pure opening mode ($x = z = 0$) one obtains

$$\frac{\gamma}{\gamma_b} > \frac{4[1 + (1-\nu)\tan^2 \Phi]}{(1 + \cos\Theta)\sin^2\Theta} = N_{\mathrm{RT}}. \tag{1.36}$$

The KTC-criterion can be improved by inserting more sophisticated estimates of IS values based on atomistic models [25, 136]. The Orowan estimate of σ_{iut} can be replaced by values of σ_{iht} based on the Morse potential [36]. These values reflect well the stress state of almost isotropic tension ($\sigma_1 = \sigma_2 = 1.6\sigma_3$) at the crack tip and, fortunately, they are also sufficiently precise as proved by recent *ab initio* calculations (see Section 1.1.3). The Frenkel formula for τ_{is} is quite satisfactory but the atomistic results are still more precise [31]. The normal/shear stress coupling can be reflected by inserting both linear and parabolic functions $\tau_{is}(\sigma_n)$ which, again, was verified by means of *ab initio* computations (see Section 1.1.4). Moreover, both the crack plane and the front positions that correspond to the many possible combinations of Miller indices related to all possible blunting slip systems are to be analyzed in order to obtain a complex picture of the intrinsic response. When taking these corrections into account, Equation 1.29 (for $\sigma_{iut} \to \sigma_{iht}$) and Equation 1.36 constitute very useful stress and energy criteria. They enable us to order crystals of pure elements and compounds according to their tendency to exhibit intrinsic brittleness (or ductility).

1.2.2 Calibration of Crystals

1.2.2.1 Models Based on Dislocation Emission

When considering Equation 1.36 and calculating the values of $\Gamma_{\mathrm{RT}} = N_{\mathrm{RT}}\gamma_b/\gamma$ for various crystals of elements and compounds, one can order the crystals with respect to their intrinsic brittleness/ductility. The values $\Gamma_{\mathrm{RT}} \geq 1$ predict intrinsic brittleness, whereas $\Gamma_{\mathrm{RT}} < 1$ means the intrinsic ductility. Such an ordering is called the calibration of the intrinsic brittleness/ductility of crystals. Rice *et al.* [135] performed such a calibration of selected metallic and ceramic elements by assuming angles Θ and Φ associated with one characteristic blunting configuration of the crack plane-slip system for each crystal. The results are displayed in Table 1.9. One can see that all the diamond

crystals and metallic crystals of bcc structure (except for alkali metals) are intrinsically brittle since their Γ_{RT} values are distinctly greater than 1. The extreme behaviour of alkali metals is not very surprising. Indeed, their fcc and bcc structure modifications have approximately the same energy and, moreover, crystals of Na and Li keep closed-packed structures even up to about 50 K [140]. On the other hand, all the fcc crystals (except for iridium) are intrinsically ductile, since their Γ_{RT} values lie close to 1. Note that this result agrees well with engineering experience of imperfect crystals and polycrystals of analyzed materials at room temperature. Here, due to the effect of thermal activation, all the Γ_{RT} values must be lower to promote the ductility. In this way, perfect bcc crystals might also cross over to the ductile state as is well known for engineering materials. When applying such a simple model of dislocation emission, however, it is not to be expected that the brittle/ductile boundary will be exactly 1. Anyway, more important information is offered just by the order of crystals according to their brittleness/ductility behaviour.

The influence of the loading mode on brittle/ductile behaviour of perfect crystals can be assessed by means of Equation 1.35 [136]. Let us consider, for example, bcc structures, where the crack lies in the $\{100\}$ plane with an adjacent slip system $\{110\}\langle 1\bar{1}1\rangle$ and the associated angles are $\Theta = 45^\circ$ and $\Phi = 35.3^\circ$. For a pure mode I ($x = z = 0, \nu = 0.3$) one obtains $\gamma/\gamma_b > 6.3$. Already a very small ratio of shear modes such as $K_{II} = K_{III} = 0.1K_I$ ($x = z = 0.1$) results in $\gamma/\gamma_b > 3.5$, i.e., to a considerable transfer of the intrinsic response towards ductility. The same behaviour is also exhibited by perfect crystals of fcc metals. On the other hand, the crystals with diamond structure remain intrinsically brittle even under high applied shear modes. Similar behaviour is typical also for single crystals containing dislocations. However, this is not necessarily the case for cracked polycrystals owing to the effect of friction produced by the crack-flank roughness (see Chapter 2 for more details).

1.2.2.2 Models Based on Ideal Strength

These models mostly utilize Equation 1.29 in terms of an extended analysis of the influence of the crack plane position in the crystal lattice. Crack plane and front directions $\{hkl\}$ and $\langle uvw\rangle$ related to all possible combinations of low Miller and direction indices ($0 \leq h, k, l, u, v, w \leq 4$) along with all possible blunting slip systems (the crack front forms an intersection of crack and slip planes) were investigated in our works [25, 136]. The slip configurations for fcc, bcc, diamond, B1 and B2 structures are shown in Table 1.10. The developed computer code contained procedures that were able to select various possible slip systems within the crystallographically equivalent set and construct associated blunting crack-slip configurations. The left-hand side of Equation 1.29 depends solely on the crystallography. Indeed, the atomistic simulations [31] have shown that the shear IS can be simply expressed as

Table 1.9 Values of the parameters Γ_{RT} and $\bar{\Gamma}_{\mathrm{KTC}}$ for investigated crystal structures

Crystal	Structure	Γ_{RT}	$\bar{\Gamma}_{\mathrm{KTC}}$	${}^{p}\bar{\Gamma}^{\varepsilon}_{\mathrm{KTC,min}}$	${}^{p}\bar{\Gamma}^{\sigma}_{\mathrm{KTC,min}}$	${}^{l}\bar{\Gamma}^{\varepsilon}_{\mathrm{KTC,min}}$	${}^{l}\bar{\Gamma}^{\sigma}_{\mathrm{KTC,min}}$
NaCl	B1		10.2	1.0	1.0	1.5	1.2
CsCl	B2		7.5	1.0	1.0	1.6	1.2
CsBr	B2		6.9	1.0	1.0	1.6	1.2
CsJ	B2		6.7	1.0	1.0	1.6	1.2
Mo	bcc	5.2	6.3	1.0	0.9	1.4	1.0
W	bcc	4.7	6.1	1.0	0.9	1.4	1.0
C	diam	4.5	6.0	1.0	1.0	1.3	1.2
LiF	B1	2.6	5.8	1.0	1.0	1.6	1.2
MgO	B1	2.9	5.0	1.0	1.0	1.5	1.2
Ir	fcc	3.6	4.2	0.9	0.7	1.1	0.7
Ge	diam	3.4	4.1	1.0	0.9	1.3	0.9
Fe	bcc	2.4	4.0	1.0	0.7	1.3	0.8
Si	diam	2.7	3.8	1.0	0.8	1.3	0.9
V	bcc	1.9	3.5	1.0	0.7	1.3	0.7
Ta	bcc	2.0	3.5	1.0	0.7	1.3	0.7
Nb	bcc	1.7	2.7	1.0	0.5	1.2	0.5
Ni	fcc	1.7	2.3	0.7	0.4	0.8	0.4
Al	fcc	1.2	2.1	0.8	0.4	0.9	0.4
Th	fcc		1.9	0.6	0.3	0.6	0.3
Pt	fcc	1.3	1.6	0.8	0.3	0.9	0.3
Cu	fcc	1.2	1.6	0.6	0.3	0.7	0.3
Ag	fcc	1.1	1.5	0.7	0.3	0.7	0.3
Na	bcc	1.2	1.4	0.7	0.3	0.7	0.3
Rb	bcc		1.3	0.7	0.3	0.7	0.3
K	bcc	1.3	1.2	0.8	0.3	0.8	0.3
Li	bcc	0.7	1.1	0.6	0.2	0.6	0.2
Au	fcc	0.9	0.9	0.7	0.2	0.7	0.2
Pb	fcc	0.8	0.9	0.6	0.2	0.6	0.2

$\tau_{is} = \kappa G$, where κ is the parameter characteristic for the particular structure and the slip system (see Table 1.3). Consequently, Equation 1.29 can be rearranged as

$$\frac{\sigma_{iht}}{G} > \frac{2\chi[1+\sin(\Theta/2)]}{\sin\Theta\cos\Phi} = N_{\mathrm{KTC}}, \tag{1.37}$$

where the exchange $\sigma_{iut} \rightarrow \sigma_{iht}$ was also performed. The left-hand side of Equation 1.37 is a ratio of material characteristics and the right-hand side (N_{KTC}) depends only on crystallography. Thus, another computer procedure was developed to calculate values N_{KTC} for all selected crack-slip configurations in all investigated structures. There is a wide range of N_{KTC} values for individual crystal structures as well as for each crystal. In the latter case, the set of blunting crystallographic configurations, labelled by N_{KTC} values, can be divided into brittle and ductile parts by the characteristic value σ_{iht}/G. This means that the intrinsic response of each crystal substantially depends

on the crack-plane position towards the basic crystallographic system. Nevertheless, one can determine a global characteristic $\bar{\Gamma}_{\mathrm{KTC}} = \bar{N}_{\mathrm{KTC}} G/\sigma_{iht}$, where $\bar{N}_{\mathrm{KTC}}$ is the mean value of N_{KTC}, averaged over all investigated configurations in a particular crystal.

Table 1.10 Slip configurations used in the model based on the ideal strength

Lattice	bcc		fcc		Diamond	B1	B2
Plane	{112}	{110}	{111}	{111}	{111}	{110}	{110}
Direction	⟨111⟩	⟨111⟩	⟨110⟩	⟨112⟩	⟨110⟩	⟨110⟩	⟨100⟩

All the studied crystal elements and compounds are ordered according to the global parameter $\bar{\Gamma}_{\mathrm{KTC}}$ in Table 1.9. One can clearly see that the ordering of crystals is very similar to that determined by using the parameter Γ_{RT} (shown in the same table). All ionic and covalent ceramic crystals can be considered to be intrinsically brittle, unlike those of fcc structure and the alkali metals. However, values of Γ_{RT} and of $\bar{\Gamma}_{\mathrm{KTC}}$ for practically all crystals are higher than 1 which infers their intrinsic brittleness at 0 K. In the case of RT criterion, the thermal activation at the room temperature is expected to produce a significant reduction of all values so that the alkali metals and fcc metals become ductile. In the case of KTC criterion, however, the ratio of ideal strengths in Equation 1.29 should not depend too much on temperature. The main reason for too high values must be sought in the strong dependence of τ_{is} on the normal stress component σ_n (see Section 1.1.3) which was not taken into account. This dependence was considered in both parabolic and linear approximations as

$$\tau_{is}(\sigma_n) = \tau_{is0}\left(1 - \sigma_n/\sigma_{iht}\right)^2,$$

$$\tau_{is}(\sigma_n) = \tau_{is0}\left(1 - k\sigma_n/\sigma_{iht}\right), \quad k \in \langle 0, 1\rangle.$$

Moreover, both the plane strain ($\sigma_1 = \sigma_2 = 1.6\sigma_3$) and plane stress $\sigma_1 = \sigma_2, \sigma_3 = 0$) conditions at the crack tip were studied. The computer procedure was completed by a routine that could select minimum values $\bar{\Gamma}_{\mathrm{KTC,min}}$ of all $\bar{\Gamma}_{\mathrm{KTC}}$ parameters related to investigated crack-slip configurations in a particular crystal. When the condition $\bar{\Gamma}_{\mathrm{KTC,min}} \geq 1$ is fulfilled, no blunting of the crack tip by shear can appear and, consequently, the crystal can be assumed to be definitely brittle. The computed parameters $\bar{\Gamma}_{\mathrm{KTC,min}}$, obtained for both the parabolic and the linear ($k = 0.5$) approximation, are also presented in Table 1.9. The upper indices ε (σ) stand for the plane strain (plane stress) case and the upper indices l (p) refer to the linear (parabolic) approximation of the dependence τ_{is} *vs* σ_n. The results show that, in the plane strain state, all ceramic and bcc crystals exhibit intrinsic brittleness

at absolute zero temperature. All fcc crystals including the bcc alkali metals indicate a ductile behaviour. It should be noted, however, that $\bar{I}_{\mathrm{KTC,min}}$ values slightly lower than 1 provide only a necessary but not sufficient condition for intrinsic ductility. In that case, indeed, a high dominance of brittle crack-slip configurations might be expected. Therefore, the borderline brittleness/ductility should rather correspond to $\bar{I}_{\mathrm{KTC,min}} \approx 0.9$. In the plane stress case, all the ionic ceramics (including covalent diamond) are predicted to behave in a brittle manner. However, crystals of Mo, W, Ge and Si also lie close to the brittle/ductile borderline. All other metals can be assumed as definitely intrinsically ductile. These results already seem to reflect plausibly the intrinsic response of crystals at 0 K. Moreover, the plane stress state prefers the ductile behaviour which is also to be expected.

In summary, the following conclusions with respect to the intrinsic brittleness/ductility of perfect crystals can be derived:

1. Diamond and all ionic ceramics are intrinsically brittle. This also holds for sufficiently large perfect crystals of Mo, W, Si and Ge (plane strain).
2. The perfect bcc crystals, except for alkali metals, lie close to the brittle/ductile borderline at absolute zero temperature. They are expected to exhibit a transition to ductile behaviour at higher temperatures similarly to the behaviour of real bcc crystals and polycrystals.
3. All perfect crystals of fcc metals, including the bcc alkalis, are intrinsically ductile in the whole temperature range.

The transient behaviour of the perfect body-centred Fe crystal was also recently verified by means of molecular dynamics simulations [141]. It should be emphasized that the brittleness/ductility behaviour of perfect crystals is in good quantitative agreement with long-term experimental experience with engineering single crystals and polycrystals containing defects. This means that this kind of behaviour is, at least partially, predetermined by the intrinsic properties of the crystal lattice.

1.3 Multiscale Model of Nanoindentation Test

Indentation tests represent a very effective tool to explore mechanical properties of materials. Besides hardness, many other characteristics such as strength, yield stress, fatigue limit and plastic strain can be approximately assessed from these tests. The nanoindentation test provides useful information about very local mechanical characteristics of the material's microstructure. However, this test also became a very promising experimental method for identification of the ideal shear strength (e.g., [142]). Due to a very small penetration depth, the stressed volume beneath the sharp nanoindenter may be free of preexisting dislocations. Moreover, this volume is usually constricted to one grain (single crystal) even in polycrystalline materials. During the nanoindentation, therefore, the increasing local shear stress can reach the ideal shear

strength value and, consequently, dislocations can nucleate in the ideal crystal lattice. Such an onset of local plastic deformation could be detected as a pop-in on the load-displacement curve by several authors [15, 143–145]. However, a physically plausible model of the nanoindentation test must be developed in order to determine the value of τ_{is} related to the pop-in load.

During the last 10 years, several models of the nanoindentation test have been published (e.g., [142,146,147]). These models utilized either the simple Hertzian solution of the stress distribution under a spherical indenter or more sophisticated multiscale approaches. The latter models can be built by using different concepts (see Preface). Hereafter, a multiscale approach that couples an indentation model based on continuum mechanics (finite elements) with material characteristics determined on both the mesoscopic (crystallography) and atomistic (*ab initio*) levels is introduced. In order to reflect sufficiently the physics of the indentation process, a plausible model of that kind must comply with several fundamental relationships and boundary conditions: (1) the *ab initio* calculations of pure ideal shear strength are to be generalized in order to reproduce correctly the stress state under the indenter – in particular, the influence of the normal stress σ_n on τ_{is} must be considered; (2) both the nonlinearity and the anisotropy of the elastic response of the ideal crystal are to be taken into account; (3) the evolution of the resolved shear stress and the normal stress on all appropriate crystallographic planes must be evaluated during the simulation; (4) a 3D finite element model of the nanoindentation process must be developed since the real stress state is quite different from that obtained from 2D models; (5) an analysis of friction forces between the substrate and the indenter should be also included.

To our knowledge, the first multiscale model including all the above-mentioned corrections was published by Krenn *et al.* [142]. The authors gave a very good interpretation of the pop-in effects in tungsten and molybdenum single crystals in terms of reaching the τ_{is} value. Unfortunately, a detailed description of all utilized computational procedures was not given in that paper. Therefore, the reported results cannot be checked and the methodology remains questionable. In our first work concerning the nanoindentation in the polycrystalline copper [146], only the first two corrections were incorporated into the model. In more recent papers [145,148] practically all the necessary corrections were already taken into account. Hereafter, the utilized computational procedures and the results of these models for copper and nickel will be briefly outlined.

1.3.1 Description of Submodels

The three-dimensional isotropic FEM model of the nanoindentation tests was performed by using the finite element code ANSYS. A frictionless spheroconical indenter with a radius of 0.2 µm (0.5 µm) in agreement with related

experiments for Ni (Cu) was pressed into a 5 μm thick substrate disc with a radius of 10 μm (see Figure 1.24). The values of the Young's modulus and Poisson's ratio of the diamond indenter were taken as $E = 1141$ GPa and $\nu = 0.07$, respectively. In the vicinity of the interface, the sphere was discretized with elements approximately 0.2 nm (0.5 nm) wide and the mesh of the substrate was refined from 0.4 mm (1 mm) at the outer edge of the disc to 0.2 nm (0.5 nm) directly beneath the indenter.

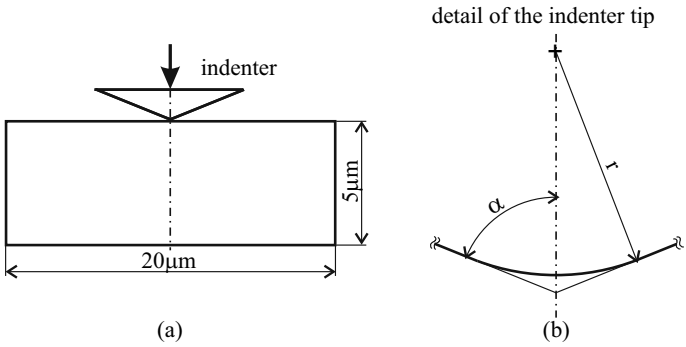

Figure 1.24 The geometrical configuration of the model: (a) cross-section of the nanoindenter and the substrate disc, and (b) scheme of the tip of the sphero-conical indenter with the semi-angle and the tip radius. Reprinted with permission from Trans Tech Publications Inc. (see page 265)

Owing to the rotational symmetry of the indentation model, only a 2D section could be analyzed as depicted in Figure 1.25. To model a contact area between the indenter tip and the specimen, the potential contact surfaces during the deformation had to be identified via a target (indenter) and the contact (substrate) elements in terms of so-called contact pairs. The elements of the substrate were, unlike those of the indenter, constrained against penetration into the opposite surface. The tangential contact stiffness based on current contact normal pressure and maximum allowable elastic slip could be updated in the frame of the ANSYS code.

The Coulomb model was utilized in the analysis involving friction. In this model, an equivalent shear stress was defined as a fraction of the contact pressure corresponding to the onset of sliding between the two surfaces. A special sticking/sliding calculation procedure determined the transitions from sticking to sliding and *vice versa* (see [148] for details).

The nonlinearity and, to a certain extent, the anisotropy of the elastic response was taken into account by a multilinear approximation of tension-compression stress-strain curves for Cu and Ni crystals. These curves were calculated from first principles in accordance with the experimental [001] indentation direction. The multilinear approximations were utilized in the ANSYS code procedure as an equivalent stress-strain dependence.

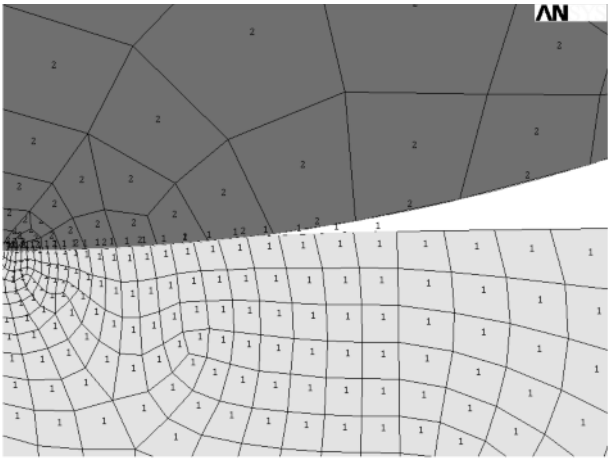

Figure 1.25 The finite element network near the contact boundary. Reprinted with permission from Trans Tech Publications Inc. (see page 265)

The function $\tau_{is}(\sigma_n)$ for the set of $\{111\}$ slip planes was also computed by means of the *ab initio* approach. Parameters of this linear dependence (see Equation 1.19) for Ni and Cu crystals can be found in Table 1.5.

The global calculation procedure simulated, step by step, the penetration of the indenter into the crystal. In order to identify the appropriate crystallographic plane in which the condition for the dislocation emission was first reached, the activity in the shear systems $\langle 112\rangle\{111\}$ was continuously tracked in stepwise calculations. The stress tensor transformation was performed to obtain all crystallographic systems related to the cylindrical symmetry. This enabled us to compute the values of τ and σ_n as functions of the rotation angle ϕ. Consequently, the maximum of the ratio $\theta_i(\phi) = \tau_i(\phi)/\tau_{is,i}(\phi)$ was searched for the entire circle going through each mesh node. The highest value of that ratio for all nodes and angles was denoted $\theta_{\max}$. Thus, the values of $\theta_{\max}$ could be related to each individual deformation step characterized by the penetration depth h.

1.3.2 Simulation of Pop-in Effects

The results obtained by using frictionless analysis were found to be practically identical with those obtained by using the model involving friction. This finding was in agreement with the conclusion already reported by Krenn *et al.* [142].

The dependence of $\theta_{\max}$ on the penetration depth h is depicted in Figure 1.26 for the nickel crystal. When the value of $\theta_{\max}$ slightly exceeds 1, the

condition for the dislocation emission can be considered to be safely fulfilled. This nearly corresponds to the depth $h = 5.5\,\text{nm}$ and the related indentation load $F = 35\,\mu\text{N}$. The associated experimental pop-in values were found to be $h_{\text{exp}} = 4.0 - 4.5$ nm and $F_{\text{exp}} = 40 - 48\,\mu\text{N}$. The following values referred to the copper crystal: $h = 12$ nm ($h_{\text{exp}} = 10 - 20$ nm) and $F = 100\,\mu\text{N}$ ($F_{\text{exp}} = 150 - 270\,\mu\text{N}$).

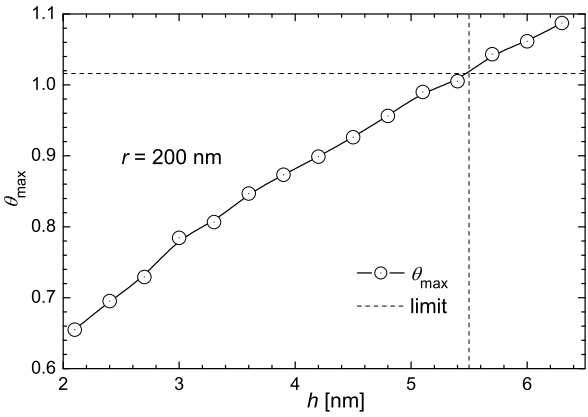

Figure 1.26 The dependence of the parameter $\theta_{\max}$ on the penetration depth h. The predicted moment of the first emission of dislocation loops corresponds to exceeding the critical value $\theta_{\max} \approx 1$ for $h \approx 5.5\,\text{nm}$

In spite of some differences in experimental and theoretical values, the results reveal that nanoindentation may serve as a very good tool for the measurement of ideal shear strength. One should note that the deviations within the range of tens of percents are highly acceptable when compared to those in the range of hundreds of percents obtained by means of other experimental methods (see Table 1.2).